[American Journal of Science, Vol. 300, January, 2000, P. 23–59]

# PRECISE GEOTHERMOMETRY ON FLUID INCLUSION POPULATIONS THAT TRAPPED MIXTURES OF IMMISCIBLE FLUIDS

ROBERT R. LOUCKS
Institute of Advanced Studies, Research School of Earth Sciences,
Australian National University, Canberra, ACT 0200, Australia

**ABSTRACT. A population of fluid inclusions that sampled boiling, condensing, effervescing, or otherwise immiscible fluids (aqueous, carbonic, or silicate melt) is potentially the most sensitive of geothermobarometers for diagenetic, hydrothermal, metamorphic, and igneous environments. This paper introduces a new, simple procedure for high-precision (to tenths of a degree usually) retrieval of crystal growth temperatures, which extends applications of fluid-inclusion studies for gradient-reconstructive hydrothermal fluid dynamics and physico-chemical modelling, and for extracting stable-isotopic fractionation factors and precise thermochemical data for end-member components of minerals by analysis of natural assemblages. In contrast to traditional estimates of the entrapment temperature ($T_{trap}$) as equivalent to the frequency mode of a homogenization temperature ($T_h$) histogram, or the lowest $T_h$ in the measured range, the new data-reduction procedure uses the frequency distribution in the entire collection of measurements spanning a large $T_h$ range, in order to determine by regression analysis the average $T_{trap}$. In theory, a population of coeval fluid inclusions that sampled immiscible fluids should have an exponential frequency distribution of the fluid-phase proportions that were trapped as heterogeneous mixtures. Thermodynamic analysis of the energy budget for nucleation and growth of an immiscible fluid phase on a growing crystal surface provides a quantitative description of how the statistical moments of the exponential frequency distribution vary with crystal/liquid/gas interfacial energies, latent heat of crystal growth, and latent heat of the fluid immiscibility reaction. Tests of the physical theory on inclusion populations in natural quartz crystals that trapped boiling hydrothermal fluids reveal well developed exponential frequency distributions with statistical properties that agree closely with thermodynamic predictions. Near the end of the paper, a practical example shows how the method is quick and easy to use, and widely applicable in metamorphic, hydrothermal and diagenetic contexts.**

**Mg-Ca-Sr-Ba carbonates and sulfates, fluorite, apatite, and scheelite precipitating from low-salinity boiling hydrothermal fluids are minerals that can only trap the aqueous liquid, not steam, in primary inclusions. They cannot provide a fluid inclusion record of hydrothermal boiling. The thermodynamic basis and examples are given.**

**Variable $T_h$ can have other causes than isothermal entrapment of immiscible fluids. Based on differences in physical mechanisms and energy budgets of the processes, statistical discriminants are derived to distinguish dispersion of $T_h$ that is due to (1) heterogeneous entrapment, (2) analytical imprecision, (3) inelastic stretching of the inclusion cavity during prior heating in nature or in the laboratory, (4) post-entrapment necking, and (5) real variation in entrapment temperature of immiscible fluids in an analyzed inclusion population.**

## INTRODUCTION

### *Geologic Fluid Immiscibility Is Common, Important, and Often Unrecognized*

Fluid-inclusion studies and direct observation have shown that immiscibility involving an aqueous liquid and a gaseous, carbonic-liquid, or silicate-liquid phase is widespread in mid- to upper-crustal igneous, metamorphic, hydrothermal, and diagenetic environments. In those regimes, recognition of evidence for fluid immiscibility is essential to understanding the mechanisms and consequences of fluid flow, for reasons such as the following. Emulsions and foams can have a bulk viscosity greater than either fluid alone, because the fluid-fluid phase interface resists deformation. Differential

*viscosity* of the fluids may be instrumental in effecting phase segregation from flowing mixtures. Differences in the effectiveness with which immiscible fluids wet mineral surfaces (that is, differential mineral–fluid *surface tension*) make a rock more permeable to one fluid than the other, with consequences for segregation of fluid phases and selective metasomatism (Yardley and Bottrell, 1988). Differential *solubility* (concentration) of chemical components in the immiscible fluids is essential for development of many kinds of economic deposits, such as sediment-hosted hydrocarbon accumulations; ortho-magmatic segregations of immiscible sulfide, oxide, or carbonate liquids from silicate melts; and magmatic-hydrothermal and "ortho-hydrothermal" ore deposits, including mercury ores precipitated from vapor segregations overlying boiling hydrothermal liquids, and metallic ores precipitated from boiled residual liquids. Differential *buoyancy* effects segregation of immiscible fluids, as in the accumulation of hydrocarbon deposits by gravitational separation from connate brine, or of hydrothermal brine exsolved from silicate melts. Differential *volume* of $H_2O$ upon exsolution from a silicate melt, or of steam/gas exsolved from water may trigger explosive volcanic, phreato-magmatic, and hydrothermal eruptions. Due to the large differential molar *enthalpy* of water and steam, boiling of aqueous fluids in a pressure gradient tends to generate very steep temperature gradients across the region of immiscibility, with dramatic effects on mineral solubilities. The mechanical, compositional and *thermal* effects of immiscible segregation of an aqueous vapor phase or a carbonic fluid from hydrothermal brine are believed to be essential aspects of ore-forming processes in all porphyry-type copper-molybdenum-gold-deposits, most porphyry-related breccia-pipe and skarn deposits, most epithermal gold-silver vein and stockwork deposits, many tin-tungsten lodes, and metamorphic slate- and greenstone-belt mesothermal gold lodes.

## *The Problem To Be Addressed*

The main line of evidence that primary fluid/melt inclusions trapped immiscible fluids is that individual inclusions in a coeval population contain varied proportions of the immiscible fluids and consequently have fluid-fluid homogenization temperatures ($T_h$) that vary widely. Confusingly, variability of phase ratios is also the main type of evidence that slowly cooled natural fluid inclusions have undergone post-entrapment necking as shown in figure 1. In that process, an initially homogeneous fluid inclusion nucleated an immiscible fluid and then fissioned afterward, producing daughter inclusions that inherited unequal proportions of the immiscible phases. Furthermore, inclusions that have been "overheated" beyond their bubble-disappearance temperature may undergo permanent stretching of the inclusion cavity, causing the stretched inclusions to homogenize to liquid at a temperature (T) substantially higher than coeval unstretched or less-stretched inclusions in the same sample. The rather easy and common confusion of these three origins of variable phase ratios and variable $T_h$ within a fluid-inclusion population, and the geologic importance of making the distinction, demonstrate the need for more reliable criteria for discriminating them.

Figure 2 compiles published histograms of liquid+gas-bubble $T_h$ for fluid-inclusion populations that are plausibly inferred by the original authors to have trapped immiscible fluids. The noteworthy feature is the pronounced skewness, with the frequency mode near the low-T end of a broad range, tapering to a high-T tail. For the reason shown in figure 3, all primary inclusions that trapped a mixture of immiscible phases should yield $T_h$ above their entrapment T's, so heterogeneous entrapment can account for the presence of some high $T_h$ values. Therefore, Roedder (1981) recommended that the $T_{trap}$ of a co-genetic inclusion population that trapped immiscible fluids may be taken as the *lowest $T_h$ value in the measured range*.

Roedder's proposal is fine in principle, but in practice there is a strong likelihood that the lowest measured $T_h$ may provide a significantly inaccurate estimate of the population's *average* $T_{trap}$, and it may in fact underestimate the $T_{trap}$ of *all* the inclusions.

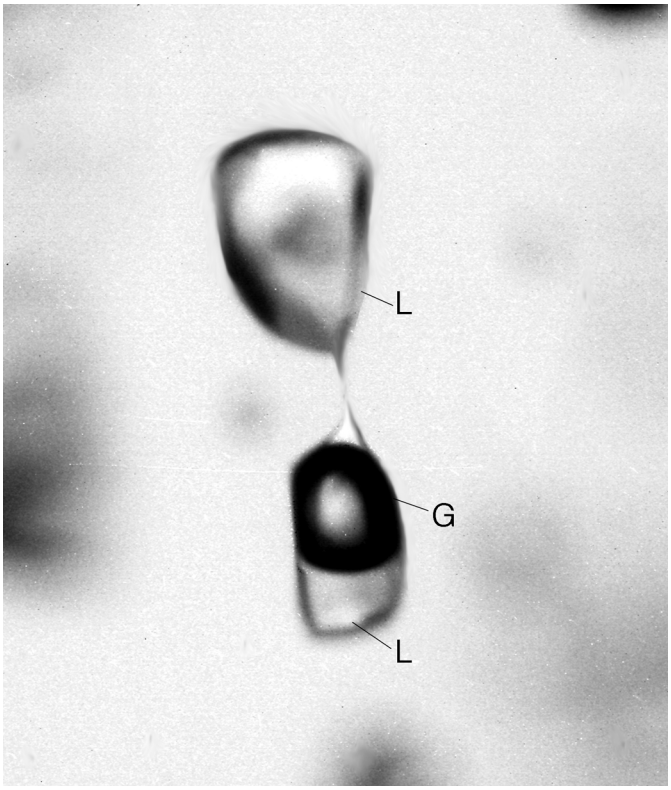


Fig. 1. An elongate primary fluid inclusion in quartz has almost completely separated into two parts, one of which is all liquid (L, top), and the other of which has a high vapor/liquid ratio (bottom). The temperature at which the liquid-rich end separates completely from its vapor-rich partner (prior to nucleating its own bubble later) is its $T_h$ value measurable in the laboratory. The same growth zone in this quartz crystal contains a high density of inclusions of varied liquid/vapor ratio that undoubtedly are un-necked primaries that trapped different mixtures of immiscible magmatic-exhalative vapor and brine. That is, there are at least two causes of variable liquid/vapor ratio among inclusions in the same growth zone of this crystal. The smoky quartz sample is from the Yankee Lode tin deposit, Mole Granite, NE New South Wales, Australia, previously described by Heinrich and others (1992) and Audétat, Günther, and Heinrich (1998). (Sample provided courtesy of Professor Christoph Heinrich.)

One reason is because mineral supersaturation and rapid crystal growth often accompany exsolution and segregation of immiscible fluids. Rapid growth is usually accompanied by high densities of lattice dislocations, primary growth strain and very irregularly shaped fluid inclusions. Highly irregular inclusions tend to become more equant later by dissolution/reprecipitation of asperities in the cavity walls, and by necking off protrusions as daughter inclusions that can be difficult to distinguish from unnecked inclusions. Another reason is that it is seldom possible in natural samples to obtain a statistically robust (that is, sizable) population of primary inclusions that were sealed precisely synchronously; inclusions sealed at slightly different times may often have substantial variations in actual $T_{trap}$. For example, Roedder (1974) reports that in one growth-zoned, color-banded sphalerite crystal from an epithermal ore vein at Creede, Colorado (where ore at higher levels precipitated from boiling fluids), the range of $T_h$ in some millimeter-wide growth bands is as much as 7°C; and across the succession of 20 growth bands, the within-band mean $T_h$ values zig-zag widely over the range 198 to 269°C, and jump abruptly by as much as 40°C across microscopically thin interfaces between growth

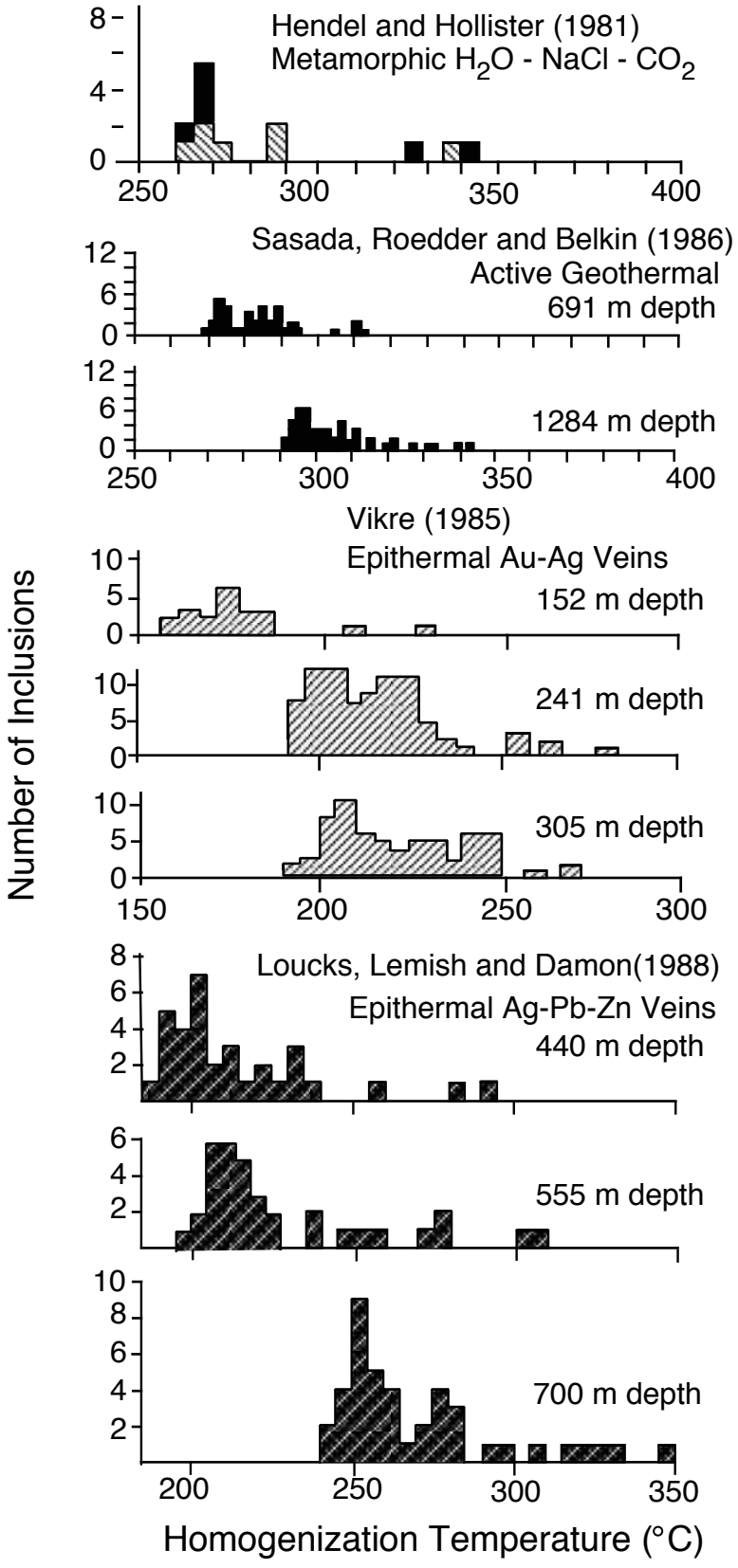
Hendel and Hollister (1981)
Metamorphic $H_2O$ - NaCl - $CO_2$
Sasada, Roedder and Belkin (1986)
Active Geothermal
691 m depth
1284 m depth
Vikre (1985)
Epithermal Au-Ag Veins
152 m depth
241 m depth
305 m depth
Loucks, Lemish and Damon(1988)
Epithermal Ag-Pb-Zn Veins
440 m depth
555 m depth
700 m depth
Number of Inclusions
Homogenization Temperature (°C)

Figure 2

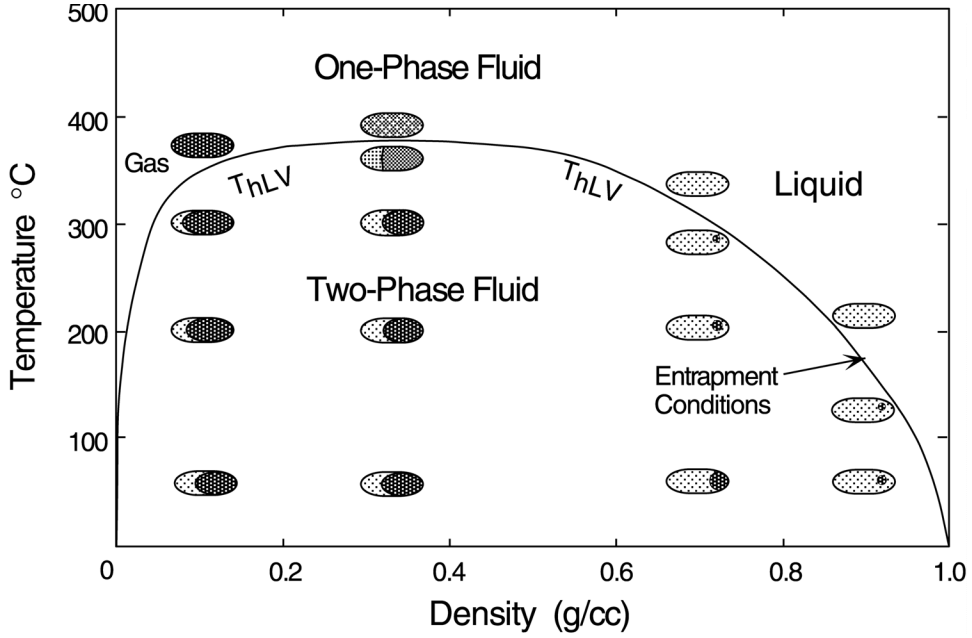


Fig. 3. Fluid inclusions that trapped various proportions of water ($\rho_L$ = 0.90 g/cc) and steam ($\rho_V$ = 0.004 g/cc) at 167°C have bulk densities of 0.10, 0.32, 0.70, and 0.90 in the cases shown. Upon heating from room temperature, the fluid inclusions homogenize at temperatures ranging from 167°C ($T_{trap}$) to 374°C ($T_{crit}$). This diagram also explains why inclusions that become necked at a temperature below their entrapment temperature yield $T_h$ different than the original entrapment temperature. (Modified from Roedder, 1967, figure 12.2.)

bands. The cause of such variation might be confusing in crystals lacking optically conspicuous growth zones. By means of excursions in the fluid's pressure and/or its content of dissolved gases or salts, fluids boiling over a similarly broad, real T range can be represented in thin growth increments of a zoned crystal. Hydrothermal explosion breccias and vein textures demonstrate that natural epizonal hydrothermal systems are commonly very dynamic with respect to excursions of fracture permeability and fluid P and T on time scales that are short compared to duration of crystal growth. In the greenschist facies of regional metamorphism, kilobar-scale cycling of fluid pressure between lithostatic and hydrostatic load is expected to be common in the depth interval of the brittle-ductile transition (Robert, Boullier, and Firdaous, 1995). Equally dynamic behavior prevails in subvolcanic hydrous magma chambers. In regions of these systems that contain immiscible fluids, P and T variations are rigidly coupled. In such dynamic environments, primary fluid-inclusion populations that represent a narrow interval of time and crystal growth may span a substantial range of actual entrapment T's.

---

Fig. 2. Several investigators have reported strongly asymmetric histograms of $T_h$ for fluid inclusion populations that were interpreted by the cited authors to represent entrapment of immiscible fluids. A characteristic feature is a frequency mode near the low-temperature end of the range and a tapering tail to higher temperatures. This compilation includes regional metamorphic fluids as well as boiling and effervescing hydrothermal fluids in an active geothermal system and epithermal Au-Ag ore deposits of Tertiary age. Note that most of the inclusions in each population have $T_h$ values well above the lowest histogram bin in the temperature range, and most are higher than the frequency mode; this means that if the measured inclusions within each population are coeval and free of irreversible modifications of volume or composition by later processes, then all of those having higher $T_h$ (most of them) must have trapped a mixture of liquid and vapor.

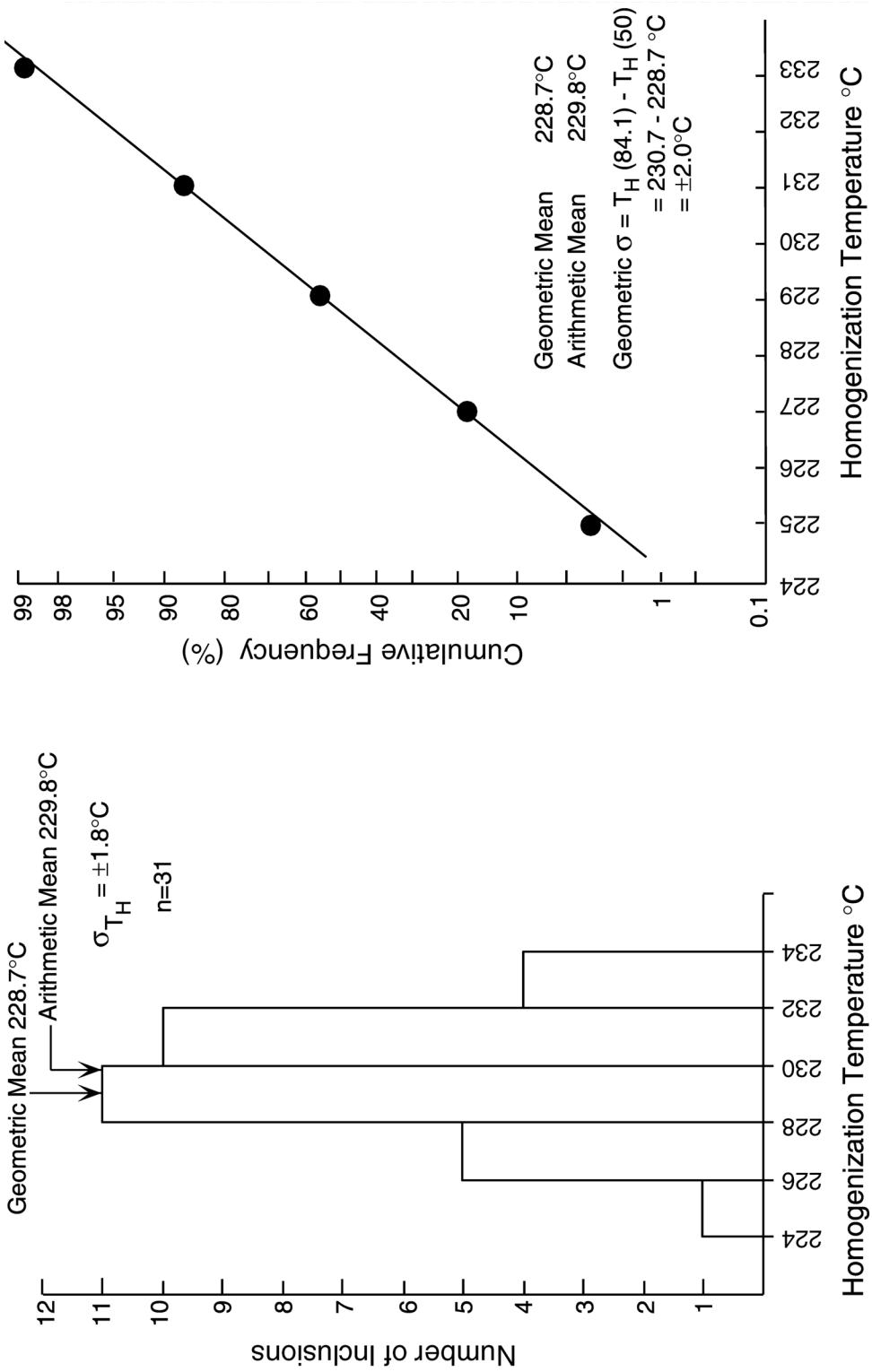
Cumulative Frequency (%)
99
98
95
90
80
60
40
20
10
1
0.1
224
225
226
227
228
229
230
231
232
233
Homogenization Temperature °C
Geometric Mean 228.7°C
Arithmetic Mean 229.8°C
Geometric σ = T_H (84.1) - T_H (50)
= 230.7 - 228.7 °C
= ±2.0°C
Number of Inclusions
12
11
10
9
8
7
6
5
4
3
2
1
224
226
228
230
232
234
Homogenization Temperature °C
Geometric Mean 228.7°C
Arithmetic Mean 229.8°C
σ T_H = ±1.8°C
n=31

Figure 4

The first question to be addressed is: How can an analyst distinguish scatter of $T_h$ that is due (1) to synchronous (isothermal) entrapment of variable proportions of immiscible fluids as primary, un-necked inclusions; (2) necking in the presence of immiscible fluids; (3) inelastic stretching during a prior heating event; and (4) real variations of $T_{trap}$ of primary un-necked inclusions? A corrollary issue is whether there is a physical basis for the histograms in figure 2 to taper to low frequencies at high T's, or whether this tapered distribution is due to sampling bias by analysts selecting inclusions "suitable" for geothermometry by rejecting ones conspicuously more vapor-rich than average. It will be shown that the physical mechanism and hence energy budgets for the enumerated processes are different, so there is a thermodynamic basis for formulating statistical discriminants that can sort the proportion of the total variation of $T_h$ that is attributable to each of these factors.

The second question to be addressed is: Having established that a population of inclusions actually trapped immiscible fluids, what is the most reliable procedure for determining the T-P conditions of entrapment? And at what level of precision or uncertainty?

## $T_H$ DISTRIBUTION IN NECKED-INCLUSION POPULATIONS

A population of necked inclusions that trapped samples of the same homogeneous liquid should be distinguished by a symmetric frequency distribution of bulk-fluid density, $\rho_B$. For a mixture of liquid (L) and gas phase (G), the material balance is $\rho_B = F_L\rho_L + (1 - F_L)\rho_G$ wherein $F_L$ is the inclusion's volume fraction of liquid. Homogenization temperatures should also have a *nearly* symmetric distribution because, except in the vicinity of the critical point, the liquid's thermal expansivity varies slowly with temperature (figure 3; this idea applies as well to the liquid-vapor solvus for brine and the immiscibility surface of carbonated brine). Therefore, the density of vapor-saturated aqueous liquid is a nearly linear function of T (to within a few percent error) over intervals up to ~100°C or so. Another reason to expect nearly symmetric $T_h$ histograms is because, to the degree that the gas approximates zero density and to the degree that the liquid's density approximates linear variation with T in the T range of interest, the $T_h$ to the liquid phase approximates linear co-variation with the bulk density of liquid-gas mixtures in a range that is symmetric about the density of the *original* parent liquid.

Figure 4 shows $T_h$ results for a co-planar swarm of natural secondary inclusions of brine in hydrothermal quartz and a normal-probability-paper plot that tests conformity of the measured cumulative frequency distribution with that of a normal frequency distribution. Figure 4 corroborates the inference that a population of coeval inclusions which includes a mixture of un-necked and necked individuals derived from the same parent liquid should have a *symmetric frequency distribution* of $\rho_B$ values and a nearly symmetric distribution of $T_h$. If after bubble nucleation, necking produces one or many generations of daughter inclusions from an ancestral volume of homogeneous liquid, the daughter population cannot give rise to a frequency distribution of $T_h$ strongly skewed toward high temperatures like those in figure 2, if the analyst selects a random, representative sample of the inclusion population.

---

Fig. 4(A) Histogram of $T_h$ for a single swarm of 31 co-planar, secondary fluid inclusions in quartz. The swarm developed according to the "necking" process in figure 1 as a single liquid-filled crack fissioned over a range of temperatures as the geologic environment cooled. (B) The cumulative frequency of $T_h$ values plots as a straight line on normal-probability coordinates, demonstrating that the distribution in (A) is Gaussian. This symmetry of fluid bulk-density or $T_h$ of daugther inclusions about the initial density value of the parent is a definitive test for discriminating inclusion populations that initially trapped a single-phase fluid and underwent necking in a two-phase field from inclusion populations in which heterogeneous entrapment of varied phase ratios is a *primary* feature.

## $T_H$ DISTRIBUTIONS ARISING FROM STRETCHING

### *They Can Taper to a High-Temperature Tail*

During heating in the laboratory, a fluid inclusion cavity undergoes changes of volume and bulk-fluid density due to (1) dissolution of material from its walls; (2) thermal expansion of the host crystal; and (3) expansion of the cavity due to compression of the host crystal by rising internal fluid pressure as the fluid expands during heating. The *a priori* assumption in fluid inclusion geothermobarometry is that such changes tend to restore the naturally cooled inclusion to its chemical and physical state at its original conditions of entrapment. However, inclusions that have homogenized to liquid undergo a steep rise of internal pressure in response to further heating, which eventually induces inelastic deformation of the inclusion cavity. When stressed beyond its elastic limit, the host mineral may rupture, with loss of some or all contents of the fluid inclusion, or the fluid inclusion may enlarge by plastic deformation of the walls without any loss of fluid. In the latter case, irreversible enlargement of an inclusion is evident by increased $T_h$ in subsequent measurements on the same inclusion.

Figure 5 shows a $T_h$ histogram for a large number of inclusions in marine-evaporite halite that precipitated from single-phase liquid. The histogram has a skewness similar to those in figure 2 that was attributed to entrapment of heterogeneous mixtures of immiscible fluids. The high-T tail of $T_h$ frequency in figure 5 is ascribed by Roedder and Belkin (1979) to *stretching* of some inclusions, including all having $T_h$ above about 50°C (E. Roedder, pers. commun., 1990). What distinguishes $T_h$ dispersion that is due to stretching from $T_h$ dispersion due to heterogeneous entrapment of immiscible fluids?

### *How to Distinguish Stretching from Heterogeneous Entrapment*

The basic equation for volume change in terms of isothermal compressibility β and isobaric thermal expansivity α—viz., $\ln V_i - \ln V_{i_o} = \beta\Delta P - \alpha\Delta T$—was modified by Zhang (1998) to describe the relative volume change, $V_i/V_{i_o}$, in a spherical liquid inclusion enclosed by a concentric sphere of elastically isotropic host mineral (for example, halite, fluorite, sphalerite). His eq (17) can be modified to express the variation of elastic strain among inclusions having the same fluid composition and density but varying initial size. The elastic strain varies with elastic moduli of the host mineral (h) and size of inclusions (i) as follows:

$$\ln \frac{V_i}{V_{i_o}} \approx \beta_h \left[ (P_o - P_{ext}) + \frac{(P_{int} - P_{ext})}{1 - (r_{io}^3/r_{ho}^3)} \right] + \alpha_h (T - T_o) + \frac{3(P_{int} - P_{ext})}{4\Gamma_h [1 - (r_{io}^3/r_{ho}^3)]} \qquad (1)$$

wherein the subscript $_o$ denotes the initial condition at $T_h$ of the undeformed inclusion; $P_{int}$ and $P_{ext}$ denote pressure inside the inclusion and outside the host crystal, respectively; $r_{i_o}$ is the undeformed inclusion's initial radius; $r_{h_o}$ is radius of the host around the inclusion (or burial depth of the inclusion within the sample); $\alpha_h$ is the host mineral's isobaric thermal expansivity, $\beta_h$ is the host's isothermal compressibility, and $\Gamma_h$ is its shear modulus. This equation says that with heating beyond $T_o$, and hence increasing deviatoric stress ($P_{int} - P_{ext}$), the percent elastic enlargement of the fluid inclusions is greatest for inclusions having the largest ratio of inclusion-radius /burial depth $r_{i_o}/r_{h_o}$. So during heating, the big inclusions and shallow inclusions reach and breach the host mineral's elastic-limit yield strength before smaller, deeper inclusions do. (Zhang has also derived a more complex formulation for elastically anisotropic crystals, such as quartz.) Plastic deformation begins when the ratio of the deviatoric stress to the ratio of

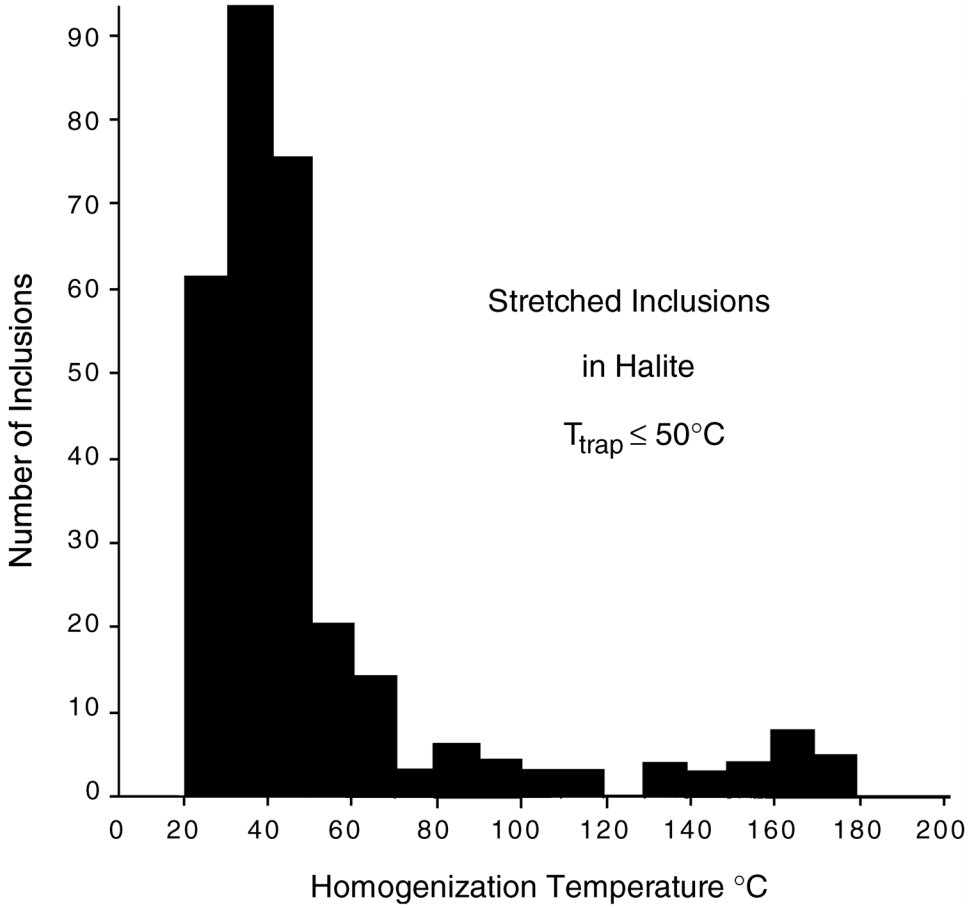


Fig. 5. Frequency distribution of $T_h$ values of fluid inclusions in halite from the marine evaporite Salado Formation, New Mexico (after Roedder and Belkin, 1979). Those authors attribute the large variation of homogenization temperature to stretching of the inclusions that homogenized above ~50°C. Note the taper of the distribution to a high-temperature tail resembling those in figure 2 that were attributed to heterogeneous entrapment. Different physical processes can cause or contribute to skewed frequency distibutions.

inclusion volume/effective volume of host armour reaches the yield strength $Y_h$ of the host mineral (Zhang, 1998, eq 28):

$$Y_h = \frac{3|P_{int} - P_{ext}|}{2(r_{io}^3/r_{ho}^3)} \tag{2}$$

That is, a fluid-inclusion wafer having a given "thickness" ($\propto r_h$) and heated to any given T and deviatoric stress ($P_{int} - P_{ext}$), has a yield strength $Y_h$ around a particular inclusion that scales inversely with the inclusion's volume: $Y_h \propto 1/r_i^3$.

### *Empirical Confirmation*

A size-strain relationship qualitatively of the sort represented by eqs. (1) and (2) was reported by Bodnar and Bethke (1984). They measured $T_h$ of inclusions in fluorite and sphalerite at $P_{ext} = 1$ atm and showed that the "overheating" (and the $P_{int}$) beyond $T_h$ that

was necessary to *initiate* stretching had an apparent logarithmic dependence on initial volume of the fluid inclusion. The degrees of overheating (hence the $Y_h$ value) needed to initiate plastic stretching varied inversely with initial size of the inclusions, but once stretching began, all the plastically stretching inclusions stretched at the same rate with continued heating. That is, the host fluorite enclosing each inclusion maintained $P_{int} - P_{ext}$ approximately constant at its initial $Y_h$ value during continued heating. (Eq. (2) only applies at the plastic yield point, not during overheating beyond it.) A sensibly constant rate of stretching means that the inclusion liquid had a sensibly constant thermal expansion coefficient $\alpha_i$ in the T interval considered, and that all inclusions stretched at the rate $dV/VdT = \alpha_i$ In a heating schedule extending well above the initial $T_h$ of a coeval population, the big inclusions that began stretching at lower T did the most stretching overall and had the greatest elevation of their final $T_h$.

This correlation between inclusion size and the elevation of $T_h$ in stretched inclusions provides an adequate discriminant to distinguish $T_h$-histogram skewness due to stretching (as in figure 5) from skewness due to heterogeneous entrapment of immiscible fluids, the inferred cause of skewness in figure 2. Assessing whether heterogeneous entrapment is indeed responsible for the tapered tail requires a thoughtful examination of the mechanisms of homogeneous and heterogeneous entrapment, the subjects of the next section.

## HOW PRIMARY INCLUSIONS GET TRAPPED

### *The Simplest Case–Entrapment of a Homogeneous Liquid*

A *primary* intra-crystalline fluid inclusion is a sample of fluid that occupied a pit on the crystal surface and was trapped by burial under subsequently precipitated growth increments of the same crystal. Pits in the crystal surface can arise by a variety of mechanisms (reviewed by Roedder, 1984, pp. 12-18). Whatever the mechanism by which a pit began its development, its deepening and sealing over to trap a fluid inclusion proceeds by the general process of differential diffusion of growth nutrients to various portions of the pit's surfaces as depicted in figure 6. During flow of a viscous fluid past a crystal surface, the fluid's velocity decreases to zero near the solid surface. Crystal growth is fed by diffusion of the nutrient chemicals through the velocity and compositional boundary layer having a thickness on the order of 100 μm in aqueous liquids or ~1mm in low-viscosity magmas (forced convection case of Kerr, 1995). Figure 6 shows schematically a diffusive concentration profile of the nutrient solute (for example, $Si(OH)^0_{4(aq)}$) in relation to pits in the surface of the growing crystal. A gradient of nutrient depletion with depth into the pit ensures that regions of the pit wall near the orifice should grow faster than regions of the pit wall farther from the orifice. This differential growth rate causes the pit to deepen, and the pit walls to steepen (figure 6B) and eventually become overturned (figure 6C), causing the orifice to shrink and then seal over, trapping a fluid inclusion.

### *Entrapment of Fluid Mixtures: A Poisson Process*

Just prior to sealing, the overhanging lip of the orifice corresponds to a geometry that facilitates appearance of an immiscible fluid phase by greatly reducing the degree of "supersaturation" required for its nucleation, as compared to homogeneous nucleation of bubbles or droplets within the parent fluid, or as compared to heterogeneous nucleation of the immiscible fluid at a planar interface between the solid and parent fluid. The thermodynamic role of surface pits or cavities in facilitating heterogeneous nucleation of the immiscible fluid is explained in the following section. For the purpose of this section, we shall take as given that heterogeneous nucleation of a bubble occurs when the cavity orifice has shrunk to a radius corresponding to that of a critically stable nucleus of the immiscible phase.

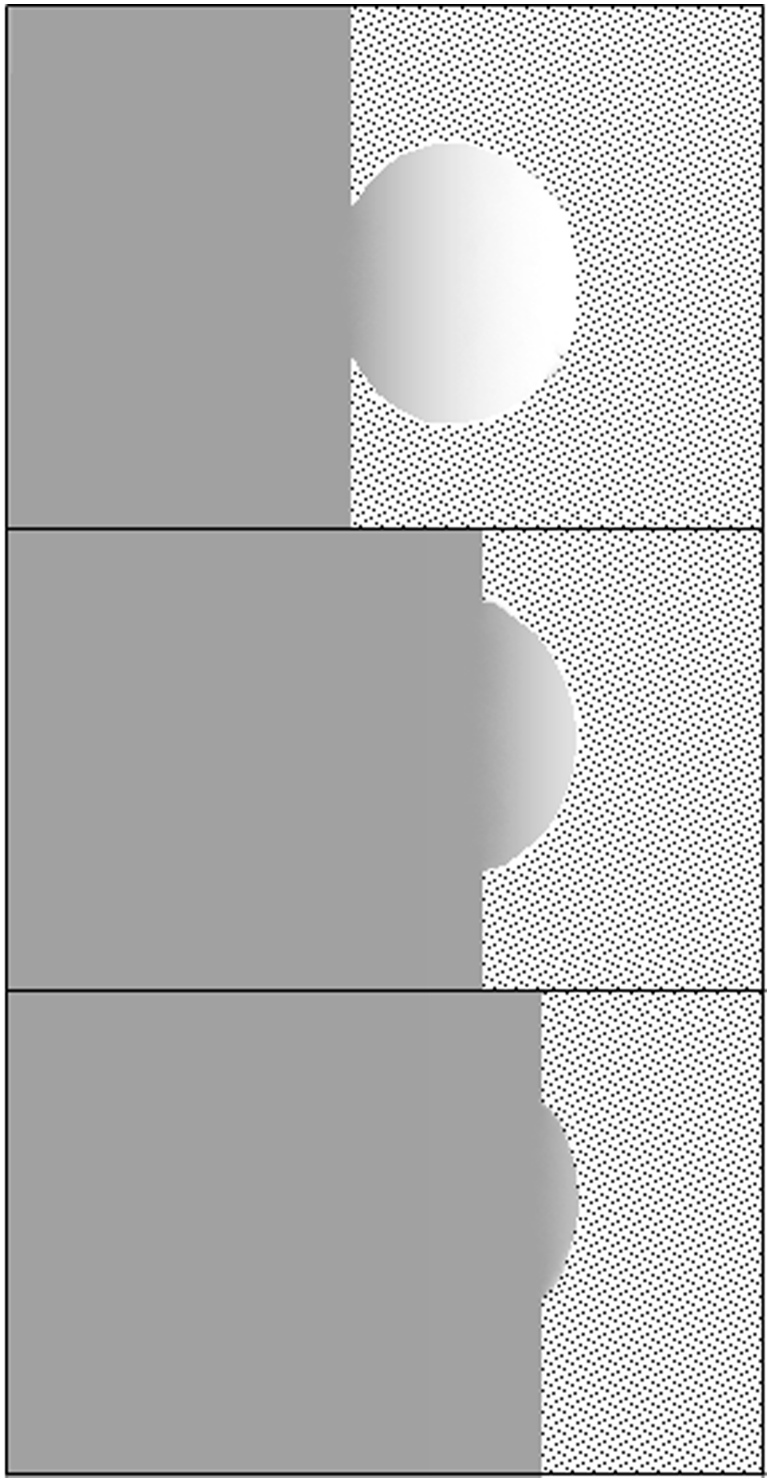


Fig. 6. Schematic illustration of the growth of a pit in a crystal surface and its eventual entrapment of a fluid inclusion, in response to the presence of a diffusive gradient (shaded) in the concentration of chemical species that feed crystal growth. The gradient of depletion toward the bottom of the pit causes slower crystal growth there and faster growth near the rim, which fosters eventual development of an orifice having an overhanging lip.

As a point of departure in this exploration, let us consider the case of quartz precipitation from *vapor-saturated* hydrothermal brine. Similar considerations will apply to other kinds of crystals precipitating in the presence of other kinds of immiscible fluids. Suppose that the hydrothermal brine's T, P, composition, and flow rate are steady during an arbitrary interval of a quartz crystal's growth. Then during the interval considered, the mass of quartz precipitated is a linear function of time, and the quantity of vapor produced from quartz's heat of precipitation is a linear function of time. In this case, *the variation within a population of contemporaneous inclusions in their proportion of entrapped vapor and liquid corresponds to variation among them in the time available for vapor growth after bubble nucleation in the surface pit and before the inclusion cavity sealed.* Let the surface pit begin developing at time $\tau_o$, nucleation of a vapor bubble occur at time $\tau_n$, and the pit seal over at time $\tau_s$, entrapping a fluid inclusion. For a population of coeval inclusions that isothermally trapped liquid + vapor mixtures, measurement of an inclusion's $T_h$ or the bulk density ($\rho_B$) of its liquid + vapor mixture is equivalent to measurement of the fraction of a pit's lifespan ($\tau_s - \tau_o$) during which a bubble was growing: $\rho_B \propto (\tau_s - \tau_n)/(\tau_s - \tau_o)$. As discussed in the next sub-section, precipitation of a unit volume of quartz supplies enough latent heat to produce a volume of steam ~40 times larger at 225°C, 30 times larger at 250°C, or 20 times larger at 275°C. So quartz precipitation in or around the cavity orifice after bubble nucleation should cause relatively rapid enlargement of the bubble. If bubble enlargement causes the bubble to protrude somewhat from the crystal surface into the ambient liquid, then the vapor would tend to shield the orifice from being capped by quartz precipitation; advance of the crystal face by continued precipitation would lead to development of an elongated capillary-like orifice to the fluid-inclusion cavity. (The development of narrow, tubular vapor-rich inclusions oriented normal to crystal faces in quartz has been attributed by Roedder (1972) to quartz precipitation around a bubble that rides the growing crystal surface outward and leaves a tubular cavity in its wake.) As latent heat is released at the growing crystal surface and part is transmitted to adjacent liquid in the cavity, more of the enclosed liquid can evaporate, enlarging the bubble inside, until the orifice neck eventually seals over, at which time the density of the entrapped liquid + vapor mixture becomes fixed. After a vapor nucleus has appeared in the cavity orifice, and a tubular neck is developing, a cavity is, on average, as likely to seal over in any particular time interval as in any other non-overlapping interval of the same duration. That is, the time interval $\tau_s - \tau_n$ is a random variable, and so is its normalized analogue, $(\tau_s - \tau_n)/(\tau_s - \tau_o)$.

A Poisson variable usually represents a count of randomly timed events that have occurred since the starting time up to time $\tau$. For a Poisson process, the waiting time to the first event is exponentially distributed, as is also the time elapsed between subsequent events, $\tau_k$ to $\tau_{k+1}$. The waiting time from nucleation of a bubble at time $\tau_n$ until the cavity seals at time $\tau_s$ may vary stochastically within the available time frame lasting from initiation of the pit at time $\tau_0$ until sealing at time $\tau_s$ . In that case, the probability that the interval $\tau_s - \tau_n$ exceeds any specified value of $\tau$ is equivalent to the complement of the *C*umulative *P*robability to time $\tau$, given by $1 - CP_{\tau_n}(\tau)$, and is equal to the probability, $p_x(0)$, that no "cavity-sealing" event has occurred in the pit in the time interval from $\tau_n$ to $\tau$. For a Poisson variable x having a probability distribution in time that is given by $p_x(x) = [(\tau/\delta)^x e^{-\tau/\delta}]/x!$, the situation of interest corresponds to (following Benjamin and Cornell, 1970, p. 243):

$$1 - CP_{\tau n}(\tau) = \frac{(\tau/\delta)^0 \exp\left[(-1/\delta)(\tau_s - \tau_n)/(\tau_s - \tau_0)\right]}{0!} = \exp\left[(-1/\delta)\frac{\tau_s - \tau_n}{\tau_s - \tau_0}\right] \qquad (3)$$

wherein the scaling factor $\delta$ is a dimensionless "dispersion coefficient" representing average time lapse between events, and $1/\delta$ is therefore a characteristic rate. The

argument is normalized to the pit's lifespan, $\tau_S - \tau_0$, making it non-dimensional for conformity with fractional frequency on the left side of the equality.

This characterization of bubble nucleation and entrapment appears to meet the three criteria that define a Poisson process (Benjamin and Cornell 1970 , p. 240). There is no violation of the requirement that the number of bubble-nucleation events or cavity-sealing events in any interval of time is independent of the number in any other non-overlapping interval of time, nor of the requirement that there is a negligible probability of multiple such events simultaneously in the same pit. The "stationarity" criterion for a Poisson process states that the probability of an event in a short interval of time is the same for all time intervals of equal length, regardless of the starting time, $\tau_n$. (The evolution of pit shape with time in figure 6 prior to attaining conditions suitable for bubble nucleation is not relevant to the stationarity criterion.) After nucleation and during development of an indefinitely elongated orifice neck, development of a seal capping it is equally likely to occur at any time, so the variable $\tau_s - \tau_n$ satisfies the stationarity criterion of a Poisson process.

## CORRELATION OF STATISTICAL AND THERMODYNAMIC ASPECTS OF ENTRAPMENT

This section examines the energy budget for formation of primary inclusions that trap immiscible fluids, including the crystal's heat of precipitation, the role of liquid/gas/crystal interfacial energies, and the energy requirements for nucleation of an immiscible fluid in pits of varied geometry on the crystal surface. The aim is to relate the physical chemistry to the mathematical form of the probability distribution of phase ratios as given by eq (3).

### *Formulation of the Independent Variables*

To represent variation of the proportions of liquid and vapor in a population of primary inclusions that trapped liquid + vapor mixtures, it is convenient to take as the independent variable the deviation of an inclusion's $T_h$ from that of an inclusion that trapped only the vapor-saturated *liquid* phase. For an errorless measurement on an inclusion that trapped only liquid, the homogenization temperature is the entrapment temperature, so the deviation variable for the general case is $T_h - T_{trap}$. Alternatively, the deviation of the bulk density of the entrapped L + G mixture from the density of the liquid phase at the entrapment P and T may be taken as the independent deviation variable–for example, $\rho_L - \rho_B$, wherein $\rho_B$ is the bulk density of the fluid inclusion, and $\rho_L$ is the density of the aqueous liquid at the entrapment T. For either choice, it is convenient to non-dimensionalize the deviation variable by ratioing it to its limiting value, $(\rho_L - \rho_{crit})$ or $(T_{crit} - T_{trap})$, wherein "crit" refers to density or temperature at the fluid's critical point. Because homogenization to the vapor phase occurs by disappearance of a liquid film wetting the walls of the cavity, the homogenization event can seldom be seen or measured accurately, so *attention will be restricted to inclusions that homogenize to the liquid phase.* The deviation variables have been formulated accordingly, so $(\tau_s - \tau_n)/(\tau_s - \tau_o)$ can be replaced by $(\rho_L - \rho_B)/(\rho_L - \rho_{crit})$ or by $(T_h - T_{trap})/(T_{crit} - T_{trap})$.

### *The Heat of Reaction for Crystal Precipitation*

Entrapment of a primary fluid inclusion requires that the host crystal be growing, not dissolving, when the inclusion seals over. Heterogeneous nucleation and growth of the immiscible fluid phase on the crystal surface is promoted if the host mineral has a crystallization heat-of-reaction, $\Delta_r H$, that is complementary in sign to $\Delta_r H$ of the exsolution reaction by which the immiscible fluid phase forms from the parent fluid. (Thermodynamic extensive variables *H, G, L, S, and V* and the equilibrium constant *K* are italicized throughout, to distinguish them from notation using the same letters in roman type for other things.) For example, exothermic precipitation of quartz can supply heat to drive endothermic evaporation of steam from brine, thereby promoting nucle-

ation and growth of steam bubbles on the growing quartz surface. In contrast, exothermic exsolution of a $CO_2$-rich fluid from brine and condensation of water from steam are thwarted on an exothermically growing quartz surface. But these exothermic exsolution reactions could transpire on an *endothermically* growing crystal–the usual case for calcite, anhydrite, apatite or scheelite precipitation at sub-critical temperatures and pressures from brines of low to moderate salinity.

*Heat of precipitation is sensitive to salinity.*–An impression of the significance of the heat of reaction for mineral precipitation may be gotten from table 1 wherein the reaction enthalpy for precipitation of one mole of quartz, calcite or barite from steam-saturated water and from steam-saturated 1-molal NaCl brine at 250°C is compared with the volume of steam (at saturation pressure, 39 bars) that could be evaporated (+) or condensed (−) by the heat of mineral precipitation. $\Delta_r H$ values in the "water" column of table 1 are the conventional standard $\Delta_r H°$ computed using the partial molal enthalpy (of formation from the elements) of each aqueous solute at infinite dilution.

TABLE 1

*Comparison of molar heats (kJ) of mineral precipitation from $H_2O$ and from 1 molal NaCl brine at 250°C and vapor-saturation pressure. By comparison with the enthalpy of evaporation of $H_2O$ from pure water and from 1 m NaCl brine at the same T and P, the volume of steam that could be evaporated (+) or condensed (−) by the mineral-precipitation enthalpy is obtained (values in parentheses)*

| Mineral | $\Delta_r H°$ ($H_2O$) | $\Delta_r H$ (1m NaCl) |
|---|---|---|
| Quartz | −21.57[a] | −21.12[a,b] |
| ($cm^3$ steam/$cm^3$ qtz) | (+27.7)[c,e] | (+30.8)[d,e] |
| Calcite | +15.95[f] | +1.67[g,h] |
| ($cm^3$ steam/$cm^3$ cct) | (−12.6)[c,e] | (−1.4)[d,e] |
| Barite | +100.23[i] | −2.53[j,k] |
| ($cm^3$ steam/$cm^3$ brt) | (−56.1)[c,e] | (+1.5)[d,e] |

[a] For the reaction $SiO^{\circ}_{2(aq)} = SiO_{2(qtz)}$

[b] $\log \gamma_{SiO_{2(brine)}} = \bar{I} * k_{SiO_{2(brine)}}$ wherein the Setchenow coefficient is $k = -0.1133 - 4.30 \times 10^{-4}\ T + 1.310 \times 10^{-6}\ T^2 - 2.333 \times 10^{-9}\ T^3$ (T in °C; data of Chen and Marshall, 1982, at 25–300°C). $\bar{I}_{SiO_2} = 1.55$ kJ/mol

[c] $H_2O$ evaporation enthalpy $\Delta_{LG}H^{\circ}_{H_2O} = 34.3$ J/$cm^3$ of steam (Haar and others, 1984)

[d] $H_2O$ evaporation enthalpy $\Delta_{LG}\bar{H}^{brine}_{H_2O} = 33.1$ J/$cm^3$ of steam (Haas, 1976)

[e] Molar volumes: quartz 22.69 $cm^3$; calcite 36.93 $cm^3$; barite 52.1 $cm^3$ (SUPCRT92, Johnson and others, 1992)

[f] For the reaction $Ca^{2+} + CO_{2(aq)} + H_2O_{(l)} = CaCO_3 + 2H^+$

[g] Reaction: $.809\ Ca^{2+} + .191\ CaCl^+ + .954\ H_2O_{(l)} + .954\ CO_{2(aq)} + .046\ HCO_3^- = CaCO_3 + 1.954\ H^+ + .191\ Cl^-$ at $P_{CO_2} = 12$ atm.

[h] $\bar{L}_j$ (kJ/mol) as follows: $CO_{2(aq)}$, −2.61; $HCO_3^-$, 9.64; $Ca^{2+}$, 36.07; $CaCl^+$, 9.30; $Cl^-$, 10.36; $H^+$, 9.89

[i] For the reaction: $Ba^{2+} + SO_4^{2-} = BaSO_4$

[j] Reaction: $.47\ Ba^{2+} + .53\ BaCl^+ + .45\ SO_4^{2-} + .55\ NaSO_4^- = BaSO_4 + .53\ Cl^- + .55\ Na^+$

[k] $\bar{L}_j$ (kJ/mol) as follows: $Ba^{2+}$, 34.64; $BaCl^+$, 9.30; $Cl^-$, 10.36; $Na^+$, 10.08; $SO_4^{2-}$, 34.90; $NaSO_4^-$, 9.13

Heats of precipitation in 1m $NaCl_{(aq)}$ are evaluated as (Pitzer and Brewer 1961, p.380–392):

$$\Delta H_T = \Delta H^\circ_T + \sum_i \nu_i \overline{L}_i = \Delta H^\circ_T - RT^2 \sum_i \nu_i \left(\frac{\partial \ln \gamma_i}{T}\right)_{P,m_i} \quad (4)$$

wherein $\nu_i$ is the stoichiometric coefficient of species i in the balanced chemical equation, and $\overline{L}_i (=\overline{H}_i - \overline{H}^\circ_i)$ is the "relative (excess) enthalpy" of solute i, equal to the difference between its partial molal enthalpy in brine and its partial molal enthalpy at infinite dilution in water. $\overline{L}_i$ values given for charged ions in the footnotes of table 1 were computed by evaluating the activity-coefficient terms ($\partial \ln \gamma_i / \partial T$) as finite-difference derivatives in the interval 249.5 to 250.5°C, taking account of the variation of true ionic strength with T, and calculating $\gamma_i$ by the extended Debye-Hückel formulation of Helgeson, Kirkham, and Flowers (1981, eq 298) with extended-term parameters $b\gamma_{NaCl}$ from Oelkers and Helgeson (1990), and with Born solvation parameters for each solute from the SUPCRT92 database (Johnson, Oelkers, and Helgeson, 1992), updated with data for $CaCl^+$ from Sverjensky, Shock and Helgeson (1997) and for $NaSO_4^-$ from Pokrovski, Schott, and Sergeyev (1995). $\overline{L}_{SiO_{2(aq)}}$ is derived from Chen and Marshall's (1982) measurements of quartz solubility in aqueous NaCl solutions. $\overline{L}_{CO_{2(aq)}}$ is evaluated from the difference in the temperature derivatives of Henry's coefficients, $K_{H(CO_2)} = f_{CO_2}/m_{CO2}$, for $CO_2$ solubility in water (W) and in 1m NaCl brine (B): $\overline{L}_{CO_{2(aq)}} = -RT^2[(\partial \ln K^W_{H(CO_2)}/\partial T) - (\partial \ln K^B_{H(CO_2)}/\partial T)]$. Values of $K_{H(CO_2)}$ are from Drummond (1981, table 1.2). Calculated equilibrium proportions of solute species provide the stoichiometric coefficients of participants in the precipitation reactions identified in the footnotes of table 1. Concentrations of the ion pairs $BaSO^\circ_4$, $CaCO^\circ_3$, and $CaHCO^+_3$ were found to be insignificant. Reaction enthalpies $\Delta H^\circ_T$ for the equilibria among aqueous solutes and minerals shown in the footnotes are calculated from the updated SUPCRT92 database.

The thermodynamic data in table 1 are closely consistent with experimentally determined solubilities of the minerals in 1m NaCl. The reaction shown for calcite precipitation from brine at 250°C has log $K = -6.461$ (SUPCRT92), which yields $m_{\Sigma Ca} = 0.00243$ at $P_{CO2} = 12$ atm, which is in excellent accord with Ellis' (1963) measurement $m_{\Sigma Ca} = 0.00240$ at $P_{CO_2} = 12$ atm at 250°C and steam saturation in 1m NaCl. For barite precipitation from 1m NaCl brine by the reaction shown, log $K = 8.733$ (SUPCRT92), which yields a calculated value $m_{\Sigma Ba} = 0.00022$ ($= m_{\Sigma SO_4}$). This value agrees closely with the measured barite solubility $m_{\Sigma Ba} = 0.00025$ in 1m NaCl at 250°C reported by Blount (1977). This accord of calculated and experimental solubilities indicates that the thermodynamic data and hence the calculated heat budgets for crystal growth and fluid unmixing are reliable.

*Endothermically precipitated minerals do not trap steam.*–Figure 7 reports $T_h$ data from a natural sample that demonstrates the influence of host-crystal precipitation enthalpy on the liquid/vapor ratios in fluid inclusions. This quartz grain and calcite grain were co-precipitated in mutual contact in the same millimeter-wide crustification band in an epithermal Ag-Au-Pb-Zn fissure-filling vein at Topia, Durango, Mexico (Loucks, Lemish, and Damon, 1988). The two frequency modes of $T_h$ in calcite are inferred to be temporally equivalent to the corresponding $T_h$ frequency peaks in the growth-zoned quartz. The correlation is supported by melting-point depressions of ice in analyzable inclusions in quartz ($T_{m(ice)} = -3.1°C \pm 0.1$ (1σ); n = 6) which are indistinguishable from values in the calcite ($T_{m(ice)} = -3.1°C \pm 0.2$; n = 6), although fluid salinities varied widely and erratically (0.2-17 wt% NaCl equiv) through the paragenetic sequence. To avoid stretching of inclusions in calcite, their $T_h$'s were measured before those in quartz, and recorded in the order of homogenization in the first heating cycle.

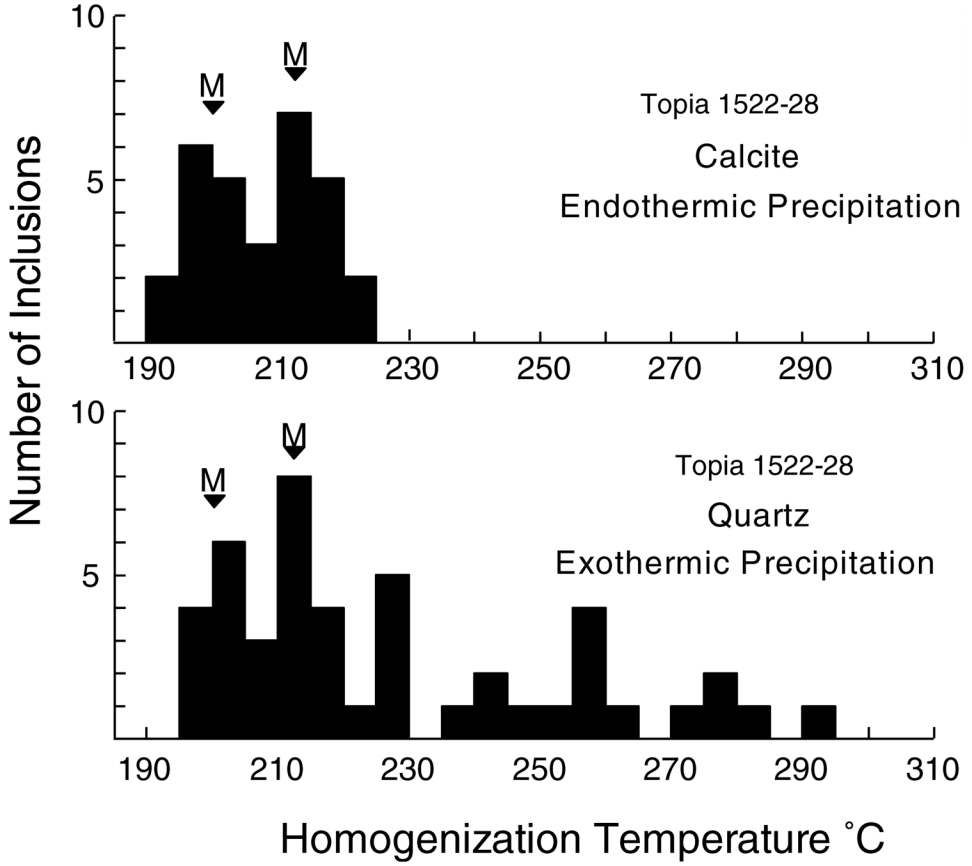


Fig. 7. Frequency distributions of $T_h$ values in mutually intergrown calcite and quartz crystals that precipitated from boiling hydrothermal fluids in an epithermal Ag-Au-Zn-Pb fissure vein at Topia, Durango, Mexico. Each distribution is bimodal, with peaks (M) at the same temperatures. Salinities of liquid-rich inclusions in calcite match those in quartz, so the two minerals are inferred to have trapped the same fluids contemporaneously. The growing calcite crystal was an energy-absorbing surface on which vapor could not survive and could not be trapped as fluid inclusions. The growing quartz crystal supplies energy promoting formation and entrapment of vapor in fluid inclusions (see table 1), so the histogram of exothermically precipitated quartz has a high-temperature tail due to heterogeneous entrapment, whereas that of coeval endothermically precipitated calcite does not.

*Incorporation of $\Delta_r H$ into eq (3).*—As indicated in table 1, the significance of the host mineral's heat of precipitation as an energy drive for fluid unmixing depends on its ratio to the heat of the liquid-gas (or liquid-liquid) unmixing reaction. This consideration implies that the enthalpy enters the formulation for the statistical dispersion coefficient $\delta$ in eq (3) in the form of the dimensionless ratio $(\Delta_{LG}H - \Delta_r H/\Delta_{LG}H)$ that is to be multiplied by the random variable $(\rho_L - \rho_B)/(\rho_L - \rho_{crit})$. Because $\Delta_r H \rightarrow \pm\infty$ at the fluid's critical point (Helgeson, 1992) and $\Delta_{LG}H \rightarrow 0$, this enthalpy ratio behaves appropriately at the critical-point limit, where the range of values accessible to $\rho_B$ goes to zero, so a vertical slope characterizes the cumulative frequency plot of $\rho_B$ values for a fluid inclusion population trapped at the critical point. A full translation of the dispersion coefficient $\delta$ into an energy budget for varying the liquid/vapor ratio and $T_h$ requires incorporation of liquid/gas/crystal interfacial energies, the subject of the next three sub-sections.

If the fluid-inclusion host mineral has $\Delta_r H = 0$ (no heat source or sink at the crystal surface to drive nucleation and growth of the immiscible fluid phase–a condition nearly met by calcite precipitation from brine in table 1; a little more salt would bring $\Delta_r H$ to zero), then the *enthalpic* role of the crystal surface in heterogeneous nucleation is indistinguishable from the case of homogeneous nucleation of the immiscible phase within the fluid.

### *The Role of Interfacial Energies in Homogeneous Nucleation*

The effect of the liquid/gas interfacial tension, $\sigma_{LG}$, on the free energy change for homogeneous nucleation of a vapor (or other gas) bubble in a liquid corresponds to the work $\sigma_{LG}A$ by the liquid in increasing its surface area by that of the bubble ($A = 4\ \pi r^2$), and the PV work by liquid in decreasing its volume by that of the bubble (Gibbs 1906, eq 554). In forming a bubble of radius r, the Gibbs energy change is

$$\Delta_f G(r) = 4\pi r^2 \sigma_{LG} - \tfrac{4}{3}\ \pi r^3 (P_G - P_L) \tag{5}$$

wherein $P_G$ is gas pressure in the bubble, $P_L$ is liquid hydrostatic pressure outside the bubble, and the surface tension $\sigma_{LG}$ ($J/cm^2$) is the Gibbs energy per unit area of the liquid-gas interface. Mechanical stability of the bubble's curved L-G interface requires that compression by the interfacial surface tension be resisted (supported) by an excess of fluid pressure inside the globule relative to the external fluid pressure, as given by Laplace's equation:

$$P_G - P_L = \frac{2\sigma_{LG}}{r} \tag{6}$$

Bubbles with a curvature more extreme than the critical radius r* are unstable because they require physically unattainable pressure differences, $P_G - P_L$. Setting r to r* in eq (6) and substituting it into eq (5) gives the variation of $\Delta_f G$ of a bubble of radius r relative to a nucleus of the smallest stable radius r*: $\Delta_f G(r) = 4\ \pi r^2 \sigma_{LG}\ [1 - (2r/3r^*)]$. $\Delta_f G(r)$ maximizes at $r = r^*$, at which value this equation becomes $\Delta_f G(r^*) = (4/3)\ \pi r^{*2} \sigma_{LG}$. Bubbles or molecular clusters with vapor-like energy (proto-nuclei) smaller than r* spontaneously collapse or disintegrate, respectively, to attain a lower (more stable) Gibbs energy. Bubbles larger than r* grow spontaneously to attain lower Gibbs energy. Homogeneous nucleation of a critically stable bubble having interface curvature r* requires that the liquid be sufficiently "supersaturated" (that is "overheated" or "underpressured") that its potential gas pressure $P_G$ exceeds the ambient pressure $P_L$ by the amount indicated in eq (6). Eq (5) says that the excess of $P_G$ over $P_L$ that is required in order to initiate nucleation corresponds to the equilibrium interfacial energy of the nucleus. As the interface curvature r increases with bubble growth, the stabilizing pressure difference $P_G - P_L$ can decrease (eq 6); the difference vanishes at a planar liquid-gas interface, for which $r = \infty$. The so-called "supersaturation" that is required for homogeneous and most heterogeneous nucleation is relative to a saturation reference state in which interfacial energy makes a negligible contribution to the system's total energy. As the fluid's critical point is approached, the liquid-vapor interfacial energy and nucleation energy vanish: $\sigma_{LG} \rightarrow 0$ in eqs (5) and (6), and $\Delta_f G(r) \rightarrow 0$.

### *Heterogeneous Nucleation on a Planar Solid Surface*

If nucleation of the immiscible fluid phase G occurs at a planar interface between a solid S and liquid L, then the relative energies of the L–G, S–G, and S–L interfaces require consideration. If the S–L interfacial energy is such that the liquid does not spontaneously wet the solid–that is, tends to contract as beads on the surface, rather than spread as a film–then a critically stable gas bubble can nucleate with a flat S-G interface

on one side (figure 8A), and an L-G interface that has a larger radius of curvature and hence a smaller "supersaturation" requirement, $P_G - P_L$, and a lower $\Delta_f G(r^*)$ than for homogeneous nucleation of a spherical bubble at the same ambient P-T conditions. Volmer (1929) showed that the work by the liquid phase in heterogeneous ("het") nucleation of a vapor bubble via the reaction $L \rightarrow G$ at a plane solid surface is diminished by a factor $\phi$, relative to the homogeneous ("hom") nucleation case under the same P-T conditions: $\Delta_f G(r^*)_{het} = \phi \times \Delta_f G(r^*)_{hom}$, where

$$\phi = 0.25\,[2 + 3[(\sigma_{SG} - \sigma_{SL})/\sigma_{LG}] - [(\sigma_{SG} - \sigma_{SL})/\sigma_{LG}]^3\} \quad (7)$$

The Young-Dupré expression, $\cos\theta = (\sigma_{SG} - \sigma_{SL})/\sigma_{LG}$, relates the interfacial energies $\sigma_{ij}$ to the contact angle $\theta$ of the L-G interface with the planar S surface (Adamson 1990, p.385) (see figure 8A). Its substitution into eq (7) gives an expression in terms of the customarily measured three-phase contact angle $\theta$:

$$\phi = (2 + 2\cos\theta + \cos\theta \sin^2\theta)/4 \quad (8)$$

If the liquid completely wets the solid surface (or in the absence of a solid surface), then $\theta = 0$, $\phi = 1$, and there is no reduction of the nucleation energy barrier $\Delta G(r^*)$ relative to the homogeneous nucleation case. Fresh, clean surfaces of most, if not all, silicate minerals are hydrophilic at subcritical T and P. In contact with a freshly formed or fractured quartz surface, water forms a small L-G contact angle $\theta \leq 25°$ at temperatures up to 90% of the absolute critical temperature; for Na-K-Mg-chloride brines, the contact angle is even smaller (Parks, 1984; Lakshtanov and others, 1995) and remains $<40°$ up to 600°C and 2000 bars (Lee, Mackwell, and Brantley, 1991). With such a small $\theta$, eq (8) does not account for the ease of steam nucleation found in practice. The resolution to that paradox lies in the role of pits in the solid surface.

### *Nucleation Facilitated by Surface Pits*

Collier (1981, p.116) examined how the radius of curvature of an L-G interface varies with the contact angle $\theta$ and with apical angle $\beta$ in conical pits. His idea is shown in

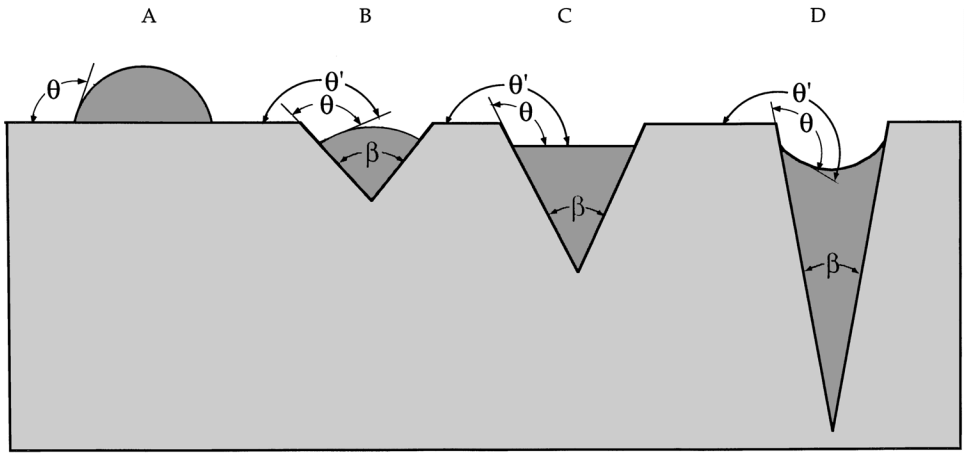


Fig. 8. Comparison of the curvature of the liquid-gas interface at a plane crystal surface (A) and in conical pits having varied apical angle $\beta$. The contact angle $\theta$ of the liquid-vapor interface with the solid (light grey shading) is measured through the liquid (unpatterned). The obtuse $\theta$ in this series is appropriate for moderately hydrophobic surfaces, such as those of sulfide minerals at hydrothermal temperatures. $\theta$ remains constant in each case, but the Gibbs energy barrier to bubble nucleation decreases in the sequence (A) to (D), as the effective contact angle $\theta'$ increases. (Modified after Collier, 1981, his figure 4.2).

figure 8B to D for a case of a relatively hydrophobic solid surface (for example, a sulfide mineral such as sphalerite) that fosters a relatively large L-G /S contact angle θ. For nucleation in cone- or pyramid-shaped surface pits, θ in eq (8) should be replaced by the "effective contact angle" θ′ defined as:

$$\theta' = \theta + \frac{180 - \beta}{2} \tag{9}$$

As the effective angle θ′ becomes more obtuse, the radius of curvature of the L-G interface increases (figure 8B and C), and then changes sign as the interface becomes *convex* toward gas (figure 8D). From eq (6), it is apparent that as the radius of curvature increases, the degree of "supersaturation", $P_G - P_L$, needed to mechanically stabilize an L-G interface (for example, bubble nucleus) decreases. If the pit shape permits a planar L-G interface for the critically stable vapor nucleus ($r^* = \infty$; figure 8C), then *no supersaturation* is needed in order to nucleate the immiscible fluid. In pits that allow still larger θ′, reversal of L-G interface curvature (negative r) allows the Gibbs energy for nucleation $\Delta G(r^*)$ to become *negative*, which means that a mechanically and thermodynamically stable vapor nucleus would form spontaneously with $P_G < P_L$ (eq 5). That is, vapor could stably nucleate from *undercooled* liquid in a surface pit, although that pressure relation would not permit survival of a free-floating bubble.

Just prior to sealing, the overhanging lip of the orifice has a form permitting development of a very obtuse effective contact angle θ′ even though the actual contact angle θ is very acute (figure 9C). Here is the key point: *the obtuse θ′ facilitates nucleation of a critically stable bubble with an orifice-spanning L-G interface having a greatly increased radius of curvature, and hence a correspondingly reduced degree of "supersaturation" ($P_G - P_L$) required for bubble nucleation (eq 5)*. With regard to crystals growing from vapor-saturated solutions, if most inclusion cavities seal by forming and then closing an overhanging orifice lip of this character, then *most fluid inclusions should nucleate a gas bubble before sealing, and trap a heterogeneous mixture of liquid and gas.* However, if the overhanging lip and the gas bubble form late in the development of the cavity, then the volumetric proportion of gas trapped with liquid in the sealed inclusion is likely to be small.

The roles of the relative interfacial energies of the L-G, S-G, and S-L surfaces in heterogeneous nucleation of a gas bubble (or globule of other immiscible liquid) on a crystal surface can be accounted for by a factor of the scaling coefficient δ (eq 3) that has the form $\Delta_f G(r^*)_{het}/\Delta_f G(r^*)_{hom}$. This is equivalent to $\phi\ \Delta_f G(r^*)_{hom}/\Delta_f G(r^*)_{hom}$ or simply ϕ, for which eq (8) is modified by incorporation of eq (9): $\phi = (2 + 2\cos\theta' + \cos\theta'\sin^2\theta')/4$.

Collecting enthalpic and surface-energy factors of the dispersion coefficient, $-1/\delta$, derived in the preceding sections, an expression in the form of eq (3) is obtained that relates thermodynamic properties of the immiscible fluids and host crystal to statistical moments of a plot of the complement of the cumulative frequency of $\rho_B$ (or $T_h$) observations on coeval primary fluid inclusions:

$$\ln\,[1 - CF(\rho_B)] \equiv \ln RCF(\rho_B) = \frac{-1}{\delta}\left(\frac{\rho_L - \rho_B}{\rho_L - \rho_{crit}}\right) = -\left[\left(\frac{(\Delta_{LG}H - \Delta_r H)}{\Delta_{LG}H}\right)\left(\frac{1}{\phi}\right)\right]\left(\frac{T_h - T_{trap}}{T_{crit} - T_{trap}}\right) \tag{10}$$

The next section of the paper examines the statistical properties of $T_h$ (or $\rho_B$) data sets representing populations of natural primary and secondary fluid inclusions having variable phase ratios. The section concludes with tests of whether the physical model described in the previous section and this one and embodied in eq (10) provides a

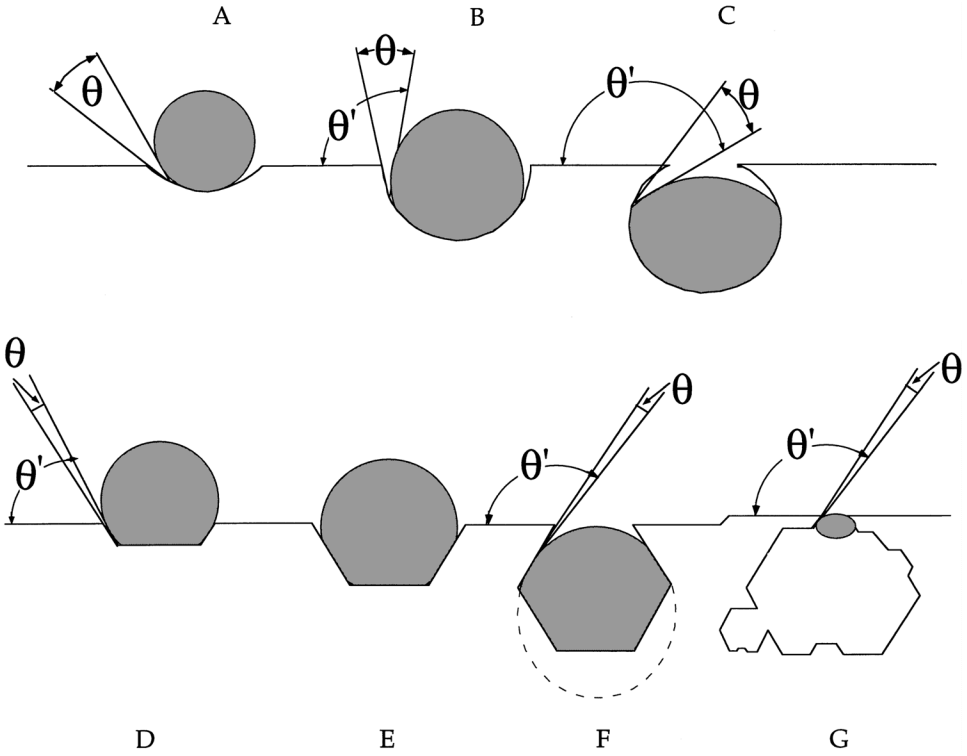


Fig. 9. The principles shown in figures 6 and 8 are combined here to illustrate how the curvature of the liquid-vapor interface and its free energy per unit area decrease as the cavity orifice develops an overturned lip. Across the upper and lower panels, the true contact angle θ remains constant, but the "effective contact angle" θ′ increases from left to right. The lower series D to G shows the 120° interfacial angles characteristic of quartz crystals (viewed down the C-axis) and the very small θ appropriate for the quartz-water interface at subcritical hydrothermal temperatures. Geometric and energetic properties of the cavity orifice are the same in panels F and G.

satisfactory representation of the data for primary inclusions and accounts adequately for the energetic aspects of the process by which growing crystals trap samples of ambient immiscible fluids.

## TESTING THE THEORY ON NATURAL FLUID INCLUSIONS

### *Samples and Analytical Procedure*

The skewed shape of the histograms in figure 2 suggests that inclusion populations that sampled immiscible fluids may have an exponential frequency distribution of fluid mass densities and vapor-liquid homogenization temperature. However, owing to the the small size of each histogram population and the poor resolution of the temporal relations among the individual fluid inclusions in any histogram, the data in figure 2 cannot be used to test definitively the exponential distribution arising from the physical model of entrapment proposed in the preceding section and embodied in eq (10). So new measurements were done on inclusions that trapped boiling hydrothermal fluids in young, undeformed epithermal veins. The samples studied are doubly polished plates of quartz from epithermal fissure-filling veins in Oligocene geothermal systems at Chloride, New Mexico (Silver Monument vein) and at Platoro, Colorado (Merrimac vein). The quartz selected is subhedral to euhedral, comb-textured, growth-banded, and largely free

of secondary inclusions. Growth bands are defined by zones rich in fluid and solid inclusions, as shown in figure 10A and B. The growth banding provides good time control for selection of large numbers of primary inclusions trapped penecontemporaneously along a particular growth band. One to three sections were cut normal to the C-axis of selected crystals, and inclusions from the same growth band in the multiple sections were analyzed with the expectation of obtaining a large enough population representing the same entrapment P-T conditions and parent-fluid composition to permit robust analysis of $T_h$ statistics. The environments that produced such dramatically zoned crystals showed more short-term variability than anticipated, but the results obtained were interpretable despite the variation within or across single growth bands.

Although gas-dominant individuals were common in all three populations of primary inclusions studied (figure 10C and D), measurements of $T_h$ were collected *only for inclusions that homogenized to the liquid phase*, because disappearance of the gas bubble is usually relatively easy to see and its T can be measured precisely. In contrast, homogenization to the gas phase occurs by disappearance of a liquid film wetting the inclusion's walls, which is usually impossible to see and prone to huge inaccuracy in its $T_h$ estimates.

Measurements of $T_h$ in a large fluid inclusion of good optical quality are reproducible, in a single analysis session, with a precision of around $\pm$ 0.1°C in the 100 to 400°C interval, using a gas-flow heating stage.[1] The precision may be expected to degrade if the compared results were obtained in multiple analysis sessions over a period of months or years, or by multiple operators on the same sample, or on multiple inclusions in the same sample, or on an inclusion of inferior optical quality.[2]

### *Is There an Exponential Distribution?*

Figure 11A to C shows histograms of fluid-inclusion bulk-fluid density, $\rho_B$ ( = $\rho_{hLG}$), for three samples in which the quartz crystal's selected growth band contained enough penecontemporaneous, primary fluid inclusions of suitable optical quality to provide reasonably robust tests of population statistics. Whether an exponential probability law governs the phase proportions in trapped liquid + gas mixtures is tested in figure 11D by re-plotting the data of figure 11A to C as a retro-cumulative (complementary-cumulative) frequency diagram on semi-logarithmic probability paper. The demonstration in figure 11D that most of the $\rho_B$ data in each sample plot as a linear array confirms that each of the three data sets has a numerically dominant sub-population that obeys an exponential

[1] All heating and freezing determinations were made on a Fluid Inc.-adapted USGS gas-flow stage (Werre and others 1979). Its thermocouple was calibrated using synthetic fluid inclusions and melting points of pure elements. During analyses, the thermocouple tip was in contact with the quartz chip and positioned within about 2 mm of the inclusions selected for study. Small chips and a slow heating schedule were used, so that all $T_{hLG}$ measurements were recorded in the order of increasing $T_{hLG}$ during a single heating run for each chip. This procedure eliminates the possibility of measurements on fluid inclusions that might have been stretched or partially decrepitated by overheating during a prior heating run.

[2] For brine inclusions homogenizing to the liquid phase, an impression of typical analytical precision by experienced operators is given by Bodnar and Sterner (1985, Table 1), who measured $T_{trap}$ of 10 or more inclusions that trapped homogeneous liquid in 14 samples of quartz containing secondary inclusions synthesized at known T. For an average of 10.7 inclusions per sample in 14 samples, the average within-sample range is 2 °C. From probability statistics for a normal distribution, that reported average range corresponds to an average standard deviation of 0.5 °C, which represents a combination of analytical error plus real variation in sealing temperature of the fluid inclusions as the furnace's temperature controller cycled through its control range. This value 0.5 °C is the same as that derived below from Roedder's (1974) $T_h$ data in individual growth bands of natural sphalerite crystals. Roedder (1974, his Fig. 1) reported $T_h$ measurements on 221 primary fluid inclusions that trapped *non-boiling* brine in 20 growth zones in a single specimen of color-banded sphalerite that was repeatedly sectioned and analyzed by several investigators using the same instrumental facility over a period of months. Within individual growth-zone colour bands, the reported $T_h$ values tend to cluster tightly, spanning 3 °C among 27 inclusions in one growth band, and 2°C in two other bands having 12 and 13 measurements, for example. From probability theory for a normal distribution of uncertainty, these reported ranges within individual bands correspond to an average standard deviation of ~0.5°C, which represents a combination of analytical error and an unresolved component of real geologic variation of $T_{trap}$ in growth bands >1mm thick.

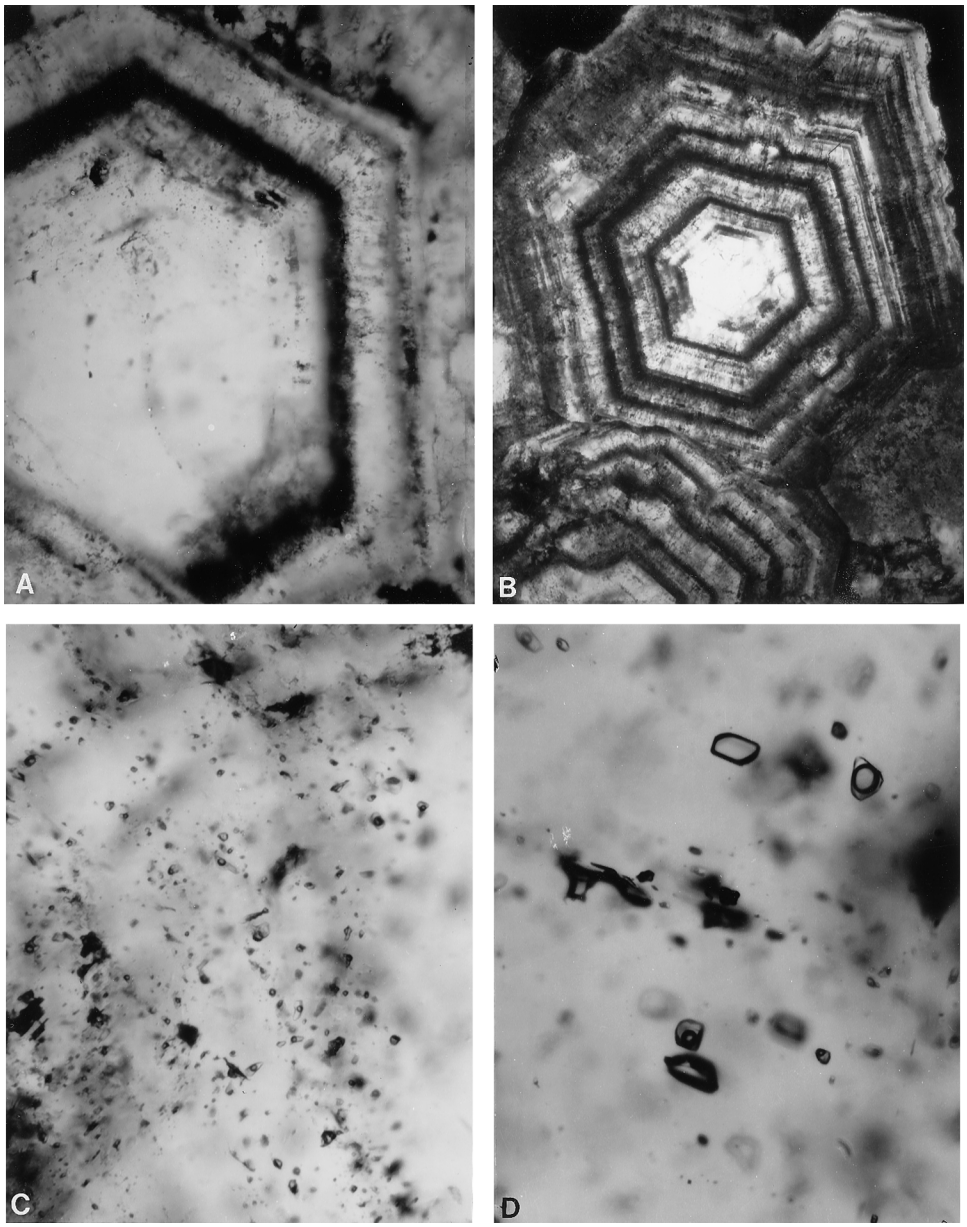


Fig. 10. Photomicrographs of sections cut perpendicular to the C-axis of growth-zoned quartz crystals that host analyzed fluid-inclusion populations. Growth zones are defined by varied abundance of fluid and solid inclusions. The samples are from epithermal fissure veins: (A) sample A13633 from the Silver Monument vein, Chloride district, New Mexico; width of frame is 2 mm; (B) sample A19218, Merrimac vein, Platoro, Colorado; width of frame is 4 mm. Photos (C) and (D) are successive enlargements of the crystal in (A), showing that the primary fluid inclusions that define growth bands have extremely variable liquid:vapor ratios indicative of heterogeneous entrapment of immiscible liquid and gas phases. Width of frame in (D) is 0.22 mm. In (D) both vapor-rich and liquid-rich fluid inclusions are clearly bounded by crystal faces (cf. ~120° θ′ angle in figure 9D); irregular dark patches near the center of (D) are opaque solids.

probability function. The misfit in figure 11D of data near the low and high ends of the range is explained in the next section.

The exponential frequency distribution of fluid-inclusion *mass density* in each histogram of figure 11A to C corresponds to an exponential distribution of liquid-gas homogenization *temperature* (upper abscissa scale), because $\rho$ and T are related by an exponential function. Combining thermal expansivity ($\alpha = (1/V)(\partial V/\partial_P = -(1/\rho)(\partial\rho/\partial T)_P$) and compressibility ($\beta = -(1/V)(\partial V/\partial P)_T = (1/\rho)(\partial\rho/\partial P)_T$) yields an integrated expression for $\rho$ as an exponential function of T and P: $\rho_h/\rho_{trap} = \exp[\beta(P_h - P_{trap}) - \alpha(T_h - T_{trap})]$.

### *Is the Thermodynamic Parameterization Correct in Eq (10)?*

The slope of the semi-logarithmic retro-cumulative-frequency (RCF $\equiv 1 - $CF) distribution has been evaluated in figure 11D for three samples by plotting the $\rho_B$ data in figure 11A to C in semi-logarithmic coordinates as suggested by eq (3). In this section, the values of the slope obtained from the least-squares linear regression of data in figure 11 are compared with theoretical thermodynamic counterparts calculated according to eq (10) for the same $P - T - m_{NaCl}$ conditions as the samples in figure 11. The comparison is a test of the appropriateness of the physical model and of the correctness of the derivation of its energetic aspects in the preceding two sections of the paper.

Table 2 shows the standard-state, excess, and overall enthalpies of the quartz precipitation reaction $SiO^0_{2(aq)} = SiO_{2(qz)}$ at the mean $T_{trap}$ and NaCl-equivalent salinities of the samples depicted in figure 11. In table 2, the overall enthalpy change of the quartz precipitation reaction is also compared with the partial molar heat of vaporization of $H_2O$ from brine of the indicated salinity, as given by Haas (1976). Critical temperatures of the brines are from Bischoff and Pitzer (1989). Experimental values of the G-L/S contact angles $\theta$ in the system quartz + NaCl-brine are not available at elevated T's, but data at 25°C summarized by Parks (1984) show that electrolyte solutes such as NaCl markedly reduce the surface energy of the quartz-water interface, enhancing the wetting of the quartz surface. So the effect of ionized aqueous chloride salts tends to counteract the experimentally demonstrated increase of $\sigma_{qz\text{-}water}$ with increasing T (Lakshtanov and others, 1995). On those grounds, it is provisionally assumed in figure 9 that, at $T_{trap}$ up to at least 270°C, the quartz-steam-*brine* three-phase contact angle remains near the 25°C value $\theta \simeq 0°$ for quartz-steam-*water* (Parks, 1984), so the average *effective* contact angle can be estimated as $\theta' \simeq 120°$ in all three quartz samples shown in figure 11. Inasmuch as quartz belongs to the hexagonal-rhombohedral crystal system, 120° is a high-probability crystallographic interfacial angle (figure 9D to G). The 120° value corresponds to an orifice-lip overhang that can provide an appropriately enlarged radius of curvature of the L-G interface to facilitate bubble nucleation at markedly reduced degrees of supersaturation (figure 9F and G). As shown in table 2, an *average* value of $\theta = 120°$ yields calculated values of the slope (compare eq (10)) as

$$\text{slope} = -\left(\frac{\Delta_{LG}H - \Delta_r H}{\Delta_{LG}H}\right)\left(\frac{1}{\phi}\right)\left(\frac{1}{T_{crit} - T_{trap}}\right) \tag{11}$$

(using $T_h$ as the abscissa variable in figure 11D) that are in satisfactory accord with slopes measured by linear regression in figure 11D. The average discrepancy between the measured slope and the theoretically predicted slope (last two columns of table 2) is just 6.8% of the predicted value.

Figure 9G suggests that just before a liquid-filled cavity seals, the orifice shrinks to a radius corresponding to the radius of a critically stable vapor-phase nucleus that is appropriate for the extant $\theta'$. This situation fosters appearance of an orifice-spanning vapor nucleus and growth of a vapor bubble inside the cavity just before it seals. The mechanism in figure 9G appears to explain the evidence in figures 2 and 11 that *most fluid*

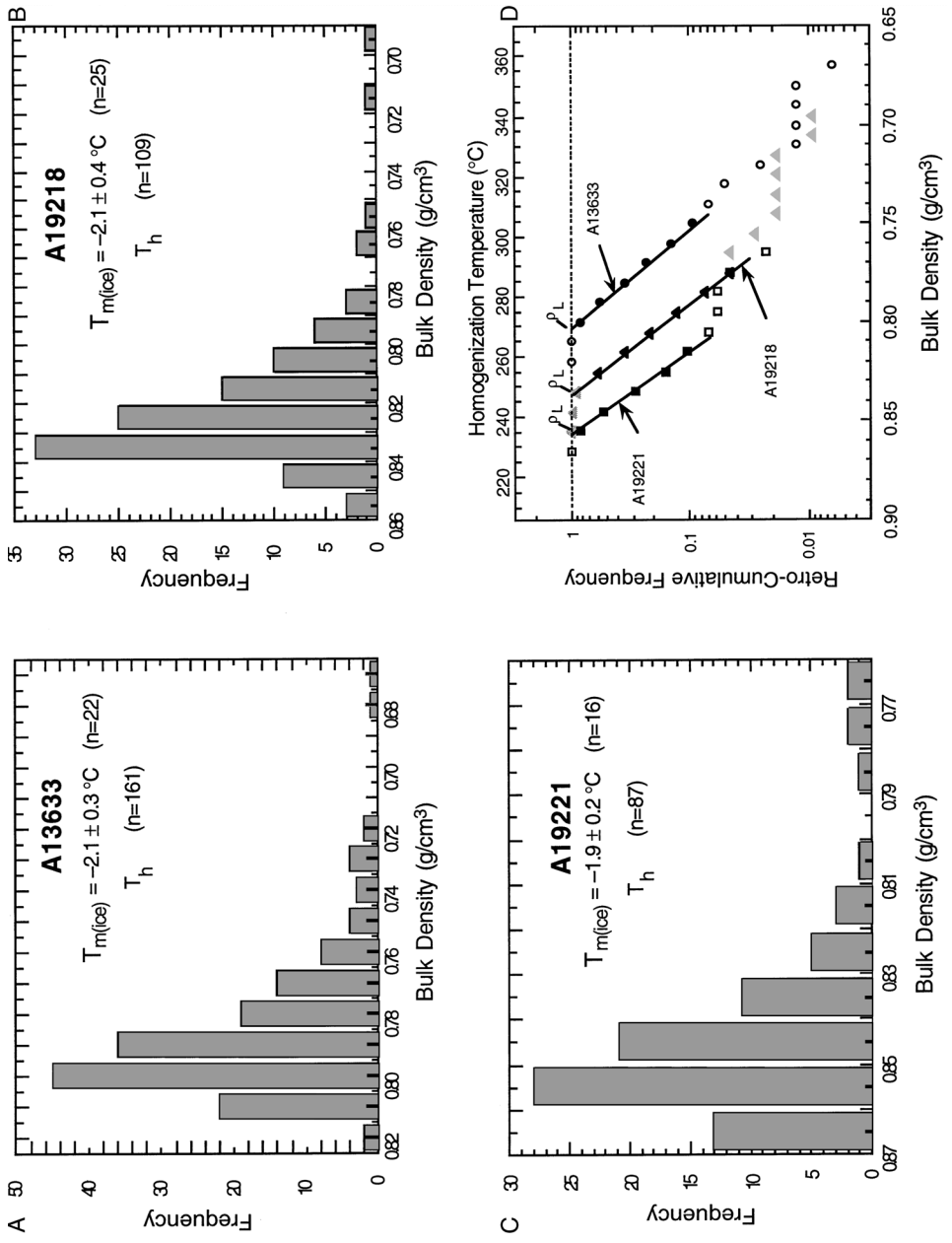
A
A13633
$T_{m(ice)}$ = −2.1 ± 0.3 °C (n=22)
$T_h$ (n=161)
Frequency
Bulk Density (g/cm³)
B
A19218
$T_{m(ice)}$ = −2.1 ± 0.4 °C (n=25)
$T_h$ (n=109)
Frequency
Bulk Density (g/cm³)
C
A19221
$T_{m(ice)}$ = −1.9 ± 0.2 °C (n=16)
$T_h$ (n=87)
Frequency
Bulk Density (g/cm³)
D
Homogenization Temperature (°C)
$\rho_L$
A13633
A19221
A19218
Retro-Cumulative Frequency
Bulk Density (g/cm³)

Figure 11

TABLE 2

*Data used to evaluate the theoretical slope according to eq (10), for comparison with empirical regression slope from fitting frequency data in figure 11A to C to the equation ln RCF($T_h$) = $-T_h/[\delta(T_{crit} - T_{trap})] +$ constant. Refer to eq (10) and figure 11D*

| Sample | [a]$m_{NaCl}$ | [b]$T_{trap}$ | $T_{crit}$ | [c]$\mathcal{L}_{SiO_{2(aq)}}$ | [d]$\Delta_r H^{\circ}_{T(qz)}$ | [e]$\Delta_r H_{T(qz)}$ | [f]$\Delta_{LG}\Pi^{brine}_{H_2O}$ | $\theta'$ | Theoretical Slope | Empirical Slope |
|---|---|---|---|---|---|---|---|---|---|---|
| A19921 | 0.56 | 228.7 | 406 | 7 | – 956 | – 963 | 1588 | 120 | – 0.065 | – 0.058 |
| A19218 | 0.625 | 247.3 | 410 | 16 | – 951 | – 967 | 1472 | 120 | – 0.065 | – 0.068 |
| A13633 | 0.625 | 269.6 | 410 | 28 | – 930 | – 958 | 1321 | 120 | – 0.078 | – 0.074 |

[a] NaCl – equivalent salinity from ice melting point.
[b] Temperatures in °C; $T_{crit}$ values from Sourirajan and Kennedy (1962), Bischoff and Rosenbauer (1985), Anderko and Pitzer (1993)
[c] Partial molal excess enthalpy of $SiO_{2(aq)}$ in J/cc of quartz; derivation in text and Eq. 4
[d] Standard enthalpy of the reaction $SiO_{2(aq)} = SiO_{2(qz)}$ (Johnson, Oelkers, and Helgeson, 1992)
[e] Standard + excess enthalpy of quartz precipitation
[f] Partial molar enthalpy of evaporation of $H_2O$ from NaCl brine of the salinity and T shown in columns 2 and 3 (Haas, 1976)

*inclusions which trap vapor-saturated liquid also trap admixed vapor, but most of them trap only a small proportion of vapor*, making the prevalence of heterogeneous entrapment difficult to recognize and fostering misinterpretation by traditional methods of data processing.

The evidence and analysis presented in this section have demonstrated that, at the time of entrapment, the proportions of liquid and vapor (or other gas) phases in inclusions that trapped mixtures is controlled by the *thermodynamic properties of the fluids and by the energetics of crystal growth and of heterogeneous nucleation* of the immiscible fluid phase. The phase proportions trapped do not represent collection by the crystal of random (or even biased) samples of the ambient two-phase fluid. The proportions of fluid phases trapped bear *no* relation to the volumetric proportion of vapor bubbles floating in the liquid. *Floating steam (or $CO_2$ or $CH_4$) bubbles cannot collide and adhere to a silicate mineral surface, displacing the brine at the surface, because such surfaces are preferentially wetted by the aqueous liquid.*

## CAUSES OF MISFIT IN THE TAILS

### *Compound Frequency Distributions Express Compound Causes of $T_h$ Dispersion*

This section shows that skewed histograms in figures 2 and 11A to C represent a dominant exponential frequency distribution superposed on a subordinate, approxi-

Fig. 11. Panels A to C illustrate the characteristic frequency distribution of bulk-fluid (liquid + vapor) density in a large population of penecontemporaneous primary inclusions occupying a single growth band in a zoned quartz crystal in three samples identified by bold-face numbers. For each sample, the NaCl-equivalent salinity of the analyzed inclusions was calculated according to Potter, Clynne, and Brown (1978) from the mean melting-point-depression of ice ($T_{m(ice)}$; the number of inclusions measured is given in parentheses). That salinity value was combined with data for brine density as a function of NaCl concentration, temperature, and pressure (Pitzer, Peiper, and Busey, 1984) to evaluate the density of the liquid at the $T_h$ of each inclusion, which is equivalent to the weighted mean density of the phase mixture that was trapped initially. The number of $T_h$ measurements in each sample is indicated in parentheses. In panel D the retro-cumulative frequency of fluid-density values (lower scale) and of $T_h$ values (upper scale) in the three samples are plotted in semi-logarithmic coordinates. (The conventional cumulative frequency is accumulated from left to right; its complement, the RCF, is accumulated from right to left.) Within the range that contains most of the data in each sample, the conformity of the values to a straight linear trend confirms that those data represent an exponential frequency distribution. In each sample, the black data points identify the subset that yields the most significant correlation and smallest uncertainty in the abscissa intercept value by least-squares linear regression. As explained in the text, extrapolation of each regression trend to its abscissa intercept at RCF = 1.00 identifies the mean *initial density of the liquid phase* (lower abscissa scale) at the *mean entrapment temperature* (upper abscissa scale) of the liquid-vapor mixtures, as follows: A13633: $r^2 = 0.9994$, $\rho_L = 0.8032 \pm 0.0004$ g/cc, $T_{trap} = 269.4 \pm 0.3$ °C ($1\sigma$); A19218: $r^2 = 0.9994$, $\rho_L = 0.8350 \pm 0.0005$ g/cc, $T_{trap} = 247.3 \pm 0.4$ °C; A19221: $r^2 = 0.9972$, $\rho_L = 0.8577 \pm 0.0008$ g/cc, $T_{trap} = 228.3 \pm 0.7$ °C.

mately Gaussian frequency distribution. The presence of a quasi-normal distribution is recognizable by the short tail on the low-T side of the frequency peak; the higher T part of that quasi-normal distribution is masked by the superposed exponential distribution. The narrow normal distribution represents normally distributed components of scatter arising from some combination of analytical error, inadvertant incorporation of a few necked inclusions in the analyzed populations, plus real oscillations or drift of geologic entrapment temperature in the analyzed populations in narrow growth bands. At the low end of the $T_h$ range, measurements that do not define the exponential distribution must be excluded from the regression to determine $T_{trap}$ of the immiscible fluids. A procedure is introduced that sorts the two superposed frequency distributions.

### *Formulation of a Test Case*

Let us devise a synthetic data set containing a mixture of normal and exponential frequency distributions, the properties of which are known *a priori* by design. Its purpose is to test the ability of a semi-logarithmic cumulative probability plot to discriminate properties of the normal-frequency distribution of actual $T_{trap}$ from properties of the exponential distribution of fluid-inclusion $T_h$ due to entrapment of phase mixtures. Table 3 shows a synthetic set of frequencies of the density of the bulk fluid (liquid + gas) in 160 fluid inclusions in each of eight successive increments of crystal growth (time stages $\tau_1$ through $\tau_8$). The density continuum is subdivided into bins 0.01 g/cm$^3$ wide. The exponential frequency distribution in each time stage is derived from the arbitrary function $f = 43.5 \exp [-43.5 (\rho_L - \rho_B)]$. Calculated frequencies are rounded off to the nearest whole number. In successive time stages, the density $\rho_L$ of the *liquid* phase of the boiling fluid is incremented or decremented by 0.01 g/cm$^3$, such that the variation of $\rho_L$ (from 0.805 in $\tau_1$ to 0.815 in $\tau_2$ and back to 0.805 in $\tau_3$ and then 0.795 in $\tau_4$) describes a *quasi-normal* frequency distribution of $\rho_L$ over the time interval $\tau_1$ through $\tau_8$. The dataset in table 3 simulates a natural process in which (1) the fluid T and the densities of the liquid and gas phases were *constant* during each growth stage, but the various fluid inclusions trapped liquid + gas mixtures in varied proportions that conform to an exponential probability distribution of the bulk density of the inclusions in each stage; and a process in which (2) the $T_{trap}$ (that is, boiling brine T) varied from one crystal-growth stage to the next.

Let us now consider the procedure for statistical interpretation of the dataset in table 3 as if it were a natural data suite in which the boundaries between crystal growth stages (time increments) $\tau_1 - \tau_8$ had been *invisible*. Considering all the eight time stages together as a temporally unresolved collection of density measurements, the row labelled "sum" in table 3 tallies the number of inclusions in each density bin (column). The underlying row labelled RCS (retro-cumulative sum) tallies the cumulative frequency in successive bins, starting at the high-T, low-density end of the distribution (right-hand column). In the underlying row labelled RCF (retro-cumulative frequency), the fractional frequency is shown, obtained by dividing the RCS value by the total number of inclusions (1280) in the dataset.

### *A Procedure for Sorting Superposed Frequency Distributions*

At its low-T high-density extremity, the collective exponential distribution overlaps the Gaussian distribution (figure 12). In the other direction, near its high-T low-density extremity, the exponential distribution's *cumulative frequency* values deviate from the ideal straight-line *cumulative probability* trend (figure 12), because counts of frequency have discrete values (integers only), whereas probability is a continuous variable. Integers generally cannot closely represent the probability at the low-frequency end of the distribution, where the exact (non-integral) probability value differs from the nearest whole number by a significant fraction of the probability value.

TABLE 3

*Synthetic data set having an exponential distribution of fluid-inclusion bulk density ($\rho_B$) in each time stage (row), and a Gaussian oscillation of brine density across the succession of time stages 1–8*

| $\rho_B$(g/cc)[a] | .815 | .805 | .795 | .785 | .775 | .765 | .755 | .745 | .735 | .725 | .715 | .705 | .695 | .685 | .675 | .665 |
|---|---|---|---|---|---|---|---|---|---|---|---|---|---|---|---|---|
| Stage $\tau$ | | | | | | | | | | | | | | | | |
| 1 | 0 | 56 | 37 | 24 | 15 | 10 | 6 | 4 | 3 | 2 | 1 | 0 | 1 | 1 | 0 | 0 |
| 2 | 56 | 37 | 24 | 15 | 10 | 6 | 4 | 3 | 2 | 1 | 0 | 1 | 1 | 0 | 0 | 0 |
| 3 | 0 | 56 | 37 | 24 | 15 | 10 | 6 | 4 | 3 | 2 | 1 | 0 | 1 | 1 | 0 | 0 |
| 4 | 0 | 0 | 56 | 37 | 24 | 15 | 10 | 6 | 4 | 3 | 2 | 1 | 0 | 1 | 1 | 0 |
| 5 | 0 | 56 | 37 | 24 | 15 | 10 | 6 | 4 | 3 | 2 | 1 | 0 | 1 | 1 | 0 | 0 |
| 6 | 0 | 0 | 56 | 37 | 24 | 15 | 10 | 6 | 4 | 3 | 2 | 1 | 0 | 1 | 1 | 0 |
| 7 | 0 | 0 | 0 | 56 | 37 | 24 | 15 | 10 | 6 | 4 | 3 | 2 | 1 | 0 | 1 | 1 |
| 8 | 0 | 0 | 56 | 37 | 24 | 15 | 10 | 6 | 4 | 3 | 2 | 1 | 0 | 1 | 1 | 0 |
| Sum[b] | 56 | 205 | 303 | 254 | 164 | 105 | 67 | 43 | 29 | 20 | 12 | 6 | 5 | 6 | 4 | 1 |
| RCS[c] | 1280 | 1224 | 1019 | 716 | 462 | 298 | 193 | 126 | 83 | 54 | 34 | 22 | 16 | 11 | 5 | 1 |
| RCF[d] | 1.0000 | .95625 | .79609 | .55938 | .36094 | .23281 | .15078 | .09844 | .06484 | .04188 | .02656 | .01719 | .01250 | .00859 | .00390 | .00078 |

Due to oscillations of the temperature of boiling brine over time, the brine density and the entire exponential frequency distribution of the trapped brine + vapor mixtures oscillates in Gaussian fashion over the succession of eight time intervals of crystal growth.

[a] The $\rho_B$ value at the head of each column is the midpoint of its histogram interval; that is, 0.815 represents the interval $0.820 > \rho_B > 0.810$.

[b] "Sum" is the summed frequencies in each density interval (column).

[c] "RCS" is the summation of "Sum" values, from right to left.

[d] "RCF" is the fractional frequency (RCS/1280) in each density interval.

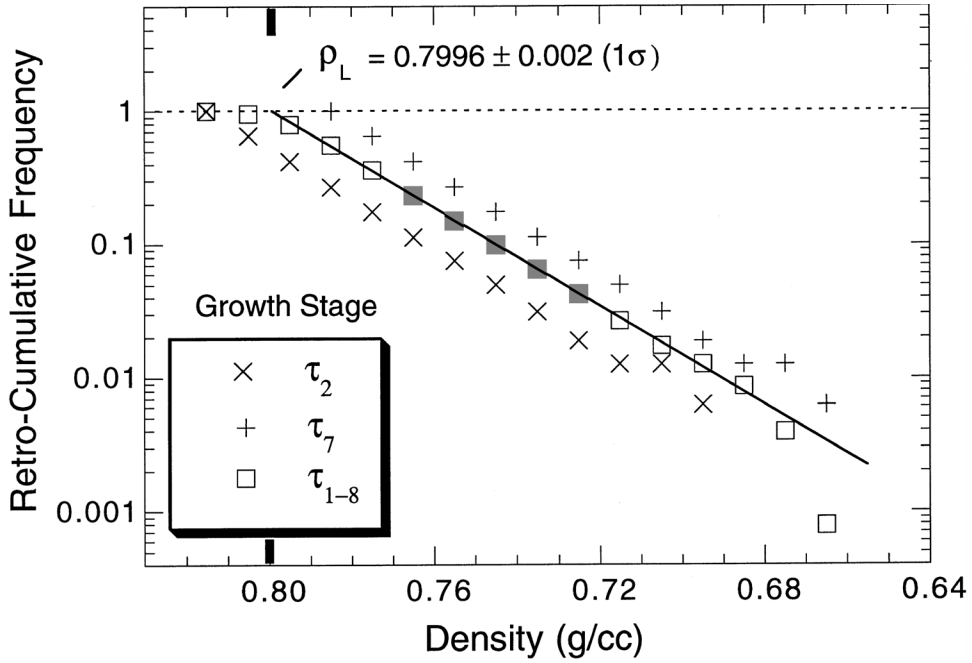


Fig. 12. The synthetic dataset in table 3 is plotted to demonstrate the ability of linear regression in semi-logarithmic coordinates to sort statistical properties of normal and exponential frequency distributions within the same data population. The shaded squares identify the subset of data for the composite time interval $\tau_1 - \tau_8$ that gives the most significant linear correlation ($r^2 = 0.99997$) of bulk-fluid density (top row of table 3) with ln RCF (bottom row of table 3). The regression equation is $\rho_B = 0.79964 + 0.02359$ ln RCF, which corresponds to $\delta = -0.02359$ (eq 11). That trend's abscissa intercept at RCF = 1.0 is $\rho_L = 0.79964$, which is an estimate of the mean density of the liquid phase at the mean entrapment temperature. This estimate of $\rho_L$ by the regression compares closely with the correct value of the mean, $\rho_L = 0.8000$ g/cc, that was built into the synthetic dataset in table 3. The × and + arrays represent the maximum and minimum in the range of temporally varying (with Gaussian frequency) liquid-phase temperature and density considered in table 3. The standard error of the abscissa intercept , $\sigma_{(\rho L)} = 0.00023$ g/cc, is evaluated according to Bevington (1969, p.114).

Here is the key point: In order to discriminate properties of the exponential frequency distribution, the range of fluid-inclusion density (or $T_h$) values over which the *exponential* function can best be fitted by least-squares is selected by iteratively truncating the extremities of the data set to find the data range that optimizes the significance level of the fit's $r^2$ (figure 12). Thus identified, *extrapolation of the exponential distribution's linear-regression trend to its abscissa intercept at a retro-cumulative frequency of 1.0 yields the best estimate of the density, $\rho_L$, of the aqueous liquid at the mean entrapment T.* In designing the table 3 example, the true mean density of the liquid phase over the time span $\tau_1$-$\tau_8$ was pre-determined to be 0.80000 g/cm$^3$, but rounding-off the exact exponential frequency probabilities to the nearest countable number generated scatter, causing the least-squares-regression equation, $\rho = 0.79964 + 0.02359$ ln RCF, to give an imperfect abscissa intercept of $\rho_L = 0.79964 \pm 0.00046(2\sigma)$. That 95% confidence interval includes the correct value of $\rho_L$. For conversion of $\rho_L$ to $T_{trap}$, a cubic polynomial in T can be fitted ($r^2 > .99999$) to Pitzer, Peiper and Busey's (1984) NaCl-brine densities. For example, if the trapped liquid were 0.625 molal NaCl brine (as in sample A19218 in figure 11), then the true mean $\rho_{L,trap} = 0.80000$ g/cm$^3$ would correspond to a true mean $T_{trap} = 271.6$°C, which compares to $T_{trap} = 271.8 \pm 0.3$°C ($2\sigma$) for the regression estimate $\rho_L = 0.79964 \pm 0.00046$ g/cm$^3$ in figure 12.

This new procedure–identifying the statistical moments of the exponential distribution by least-squares regression, and then extrapolating the regression trend to its abscissa intercept at RCF = 1.0 to find the limiting value of density or temperature that represents the entrapment conditions–can improve by at least an order of magnitude the typical precision of fluid inclusion geothermometry (and hence vapor-pressure paleobarometry), compared to procedures previously in general use on fluid-inclusion populations that sampled immiscible fluids. It also provides a robust measure of the uncertainty in the geothermometry. And the calculations are quick and easy, as illustrated by a practical example near the end of the paper. Whole $T_h$ datasets comprising just 20 inclusions commonly provide a geothermometry precision near ±1°C (standard error of the abscissa intercept value).

### *The Problem with the Frequency Mode as an Estimate of Mean $T_{trap}$*

Figure 13 employs another synthetic data set to consider the effects on the frequency histogram of mixing a temporal succession of sub-populations of primary fluid inclusions that trapped phase mixtures of fluids that were effervescing over a real range of temperature during precipitation of an arbitrarily thin growth interval of a single crystal. For the sake of conceptual clarity, asymmetric frequency distributions of the type illustrated in figures 2 and 11 are represented in figure 13 simply as a triangular distribution for each time (precipitation) increment of crystal growth. In the case illustrated, the lowest temperature in the time-integrated, *cumulative* range substantially under-estimates the mean $T_{trap}$. The *frequency mode* substantially *over-estimates* the mean $T_{trap,}$ and is about as poor an indicator of mean $T_{trap}$ as the lowest value in the cumulative range. Thus, even with a perfectly calibrated thermocouple and meticulous laboratory technique, the accuracy of these geothermometric estimators is likely to be more than an order-of-magnitude poorer than the analytical precision of ~±0.3°C, as illustrated in figure 14 using high-quality data reported by Sasada, Roedder and Belkin (1986).

## HETEROGENEOUS ENTRAPMENT IS MORE PREVALENT THAN PREVIOUSLY THOUGHT

The histograms in figures 2 and 11 demonstrate that, in populations of primary fluid inclusions that trapped boiling or effervescing hydrothermal brines, *most of the inclusions that homogenize to the liquid phase trapped a heterogeneous mixture of liquid +vapor*. This finding contradicts statements in the literature that admixed vapor is seldom trapped with the vapor-saturated liquid. In a general discussion of phase ratios in inclusions that trapped boiling hydrothermal fluids, Roedder (1984, p. 31) states "Small amounts of liquid are rather commonly (but not always) trapped with the steam, and more rarely, small amounts of vapor (that is, a small bubble) are trapped with the liquid." Bodnar, Reynolds and Kuehn (1985, p. 81) are more emphatic on the point: "Vapor-rich inclusions almost always trap some liquid along with the vapor, whereas liquid inclusions almost never trap any vapor along with the liquid." In support of that statement, they cite features of inclusions synthesized by Bodnar, Burnham and Sterner (1985).

### *Comparison with Synthetic Fluid Inclusions in Cracked Quartz*

In that study, cylindrical quartz cores were cracked, then sealed with NaCl brine in platinum capsules and then loaded in cold-seal pressure vessels and brought to the run T and P in the liquid + vapor stability field. The quartz cores were at least partly immersed in brine that coexisted with a static vapor phase occupying the top of the capsule. During the runs, the fluid-filled cracks healed, entrapping planar swarms of synthetic secondary inclusions. In addition, some primary inclusions were trapped in new quartz overgrowths that precipitated on the quartz core. Bodnar, Burnham and Sterner (1985, p. 1865) state that unlike the secondary inclusions, in most experiments "inclusions in the overgrowths are the vapor-rich type; very rarely are the halite-bearing [brine] type seen as primary inclusions . . . This observation has important implications for the

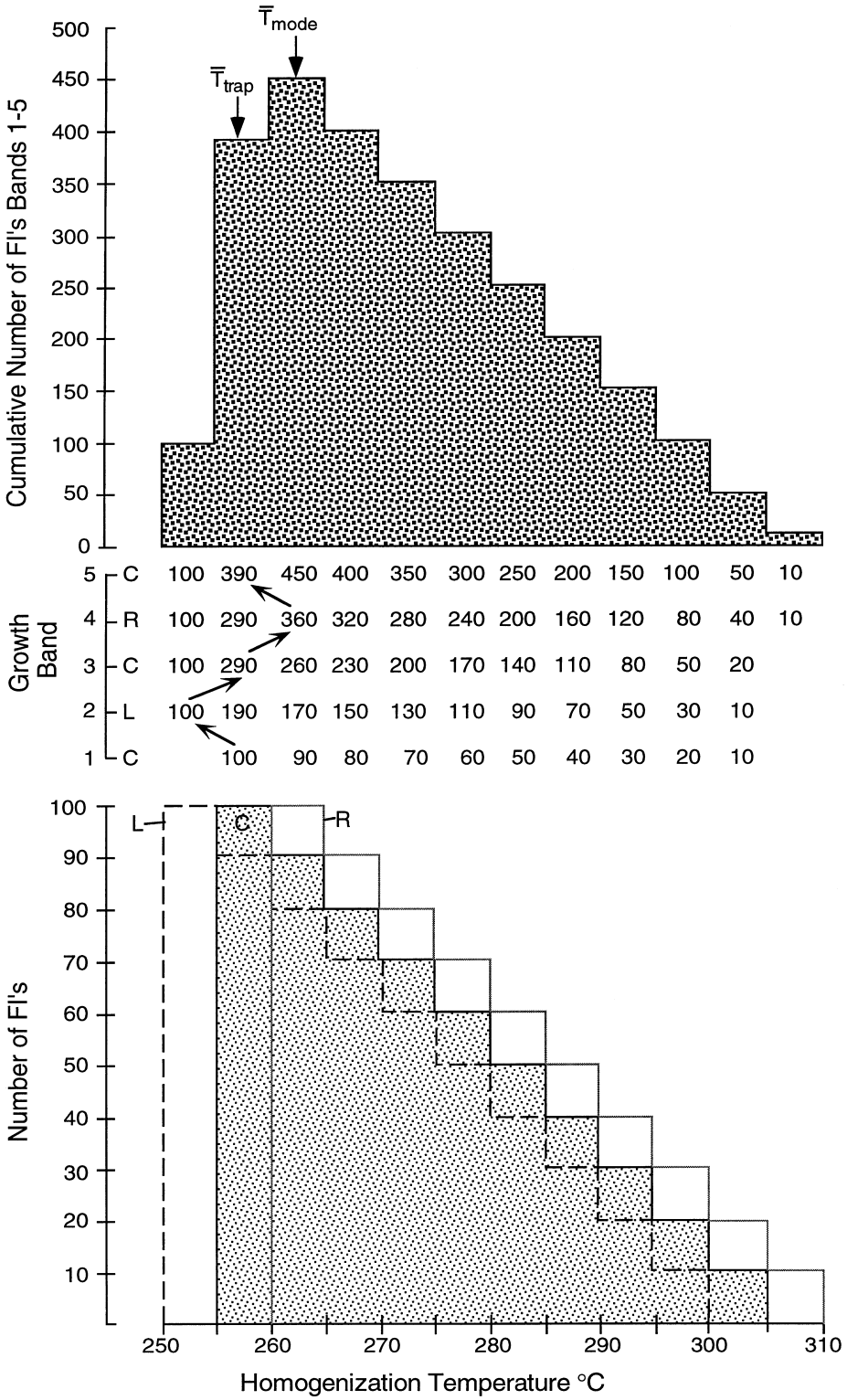
$\overline{T}_{mode}$
$\overline{T}_{trap}$
Cumulative Number of Fl's Bands 1-5
500
450
400
350
300
250
200
150
100
50
0
Growth Band
5 C 100 390 450 400 350 300 250 200 150 100 50 10
4 R 100 290 360 320 280 240 200 160 120 80 40 10
3 C 100 290 260 230 200 170 140 110 80 50 20
2 L 100 190 170 150 130 110 90 70 50 30 10
1 C 100 90 80 70 60 50 40 30 20 10
L
C
R
Number of Fl's
100
90
80
70
60
50
40
30
20
10
250
260
270
280
290
300
310
Homogenization Temperature °C

Figure 13

formation of various types of high-temperature ore deposits because it suggests that these relatively low-density, low-salinity fluids [vapor] are capable of transporting and depositing significant quantities of quartz". On the contrary, exothermic precipitation of the quartz *overgrowths* provided a heat-generating substrate driving vapor nucleation. As shown in Table 1, precipitation of *1 cm³ of quartz* at 250°C, for example, releases enough heat to evaporate 0.66 $cm^3$ of water to make *28 cm³ of steam* ($\rho = 0.020$ $g/cm^3$; Haar, Gallagher, and Kell, 1984). Bodnar, Burnham, and Sterner (1985) failed to consider the heat released by quartz precipitation. Prevalence of vapor-rich primary inclusions in the overgrowths does not indicate that quartz precipitated from vapor, in which its solubility at run conditions is about 2.5 orders of magnitude less than in the associated liquid phase (Helgeson, 1992, his figure 2).

*Synthesis in Cracked Quartz Does Not Replicate Energetics of Primary Inclusion Entrapment.*–The pre-cracked-quartz technique for hydrothermally synthesizing fluid inclusions, pioneered by Shelton and Orville (1980) and much imitated since, usefully replicates many features of natural inclusions, but the energetics of entrapping primary inclusions is not one of them. Capillarity should have caused fissures in the pre-cracked quartz to be permeated with liquid prior to the run-up to a T and P in the two-phase field. Generation of a vapor phase within the capsule does not require that it be generated within all of the liquid-filled cracks inside the rigid crystal. On the contrary, nucleation would occur where the least PV work is required. And because aqueous liquid is the quartz-wetting phase, relative to vapor, capillarity could have excluded vapor from many or most cracks. To the extent that conversion of a fluid-filled crack to a plane of secondary inclusions occurs by micrometer-scale redistribution of silica (and hence enthalpy) by complementary dissolution and reprecipitation along the crack walls, the reduction of surface energy is thermally inconsequential, and *crack healing is an enthalpy-conserving process.* The enthalpy conservation that accompanies quartz redistribution during sealing of secondary inclusions in pre-cracked quartz does not replicate the large net heat production on a growing quartz crystal face, shown in table 1. The similar and complementary magnitudes of values in table 2's enthalpy columns for steam evaporation ($\Delta_{LG}\overline{H}^{brine}_{H_2O}$) and net precipitation (rather than micrometer-scale redistribution) of quartz ($\Delta_r H_{T(qz)}$) prove beyond doubt that the heat of crystal precipitation is the main component of the energy budget for entrapment of heterogeneous liquid+vapor mixtures–a conclusion reinforced by the $T_h$ histograms for quartz and calcite in figure 7.

## SUMMARY

Geologic environments in which hydrothermal fluid immiscibility and phase segregation are common are in most cases prone to rapid crystal growth. Fast growth fosters entrapment of highly irregular inclusions that are susceptible to later necking as the

Fig. 13. In the bottom panel, skewed $T_h$ histograms of the type in figure 2 are represented schematically by three triangular frequency distributions (solid, dashed, and gray outlines) that are staggered along the abscissa and labelled L (left), C (center), and R (right). In each of the three histograms, the frequency mode represents the entrapment temperature of the whole inclusion population contained in each histogram. $T_h$ values to the right of the peak represent effects of entrapping (at the same temperature) heterogeneous mixtures of liquid and vapor in varied proportions. Staggering of the distributions (C, L, R) along the horizontal axis represents symmetric temperature oscillations (± 5 °C about the mean) during 5 successive increments of crystal growth in which $T_{trap}$ (and histogram location) oscillates in the sequence 257 → 252 → 257 → 262 → 257, shown as C → L → C → R → C along the left-hand side of the central panel containing the number array. In the number array, *arrows* track the migrations of the fluid-inclusion *entrapment temperature* in consecutive crystal growth increments labelled "band 1", etc. Rows labelled by growth band in the number array contain the summed frequency of the $T_h$ values in the current and underlying bands. Row 5 contains the summed frequencies in bands 1-5, and is plotted in histogram form in the top panel. The message in the top histogram is that the overall mean entrapment temperature ($\overline{T}_{trap}$) and the frequency mode ($\overline{T}_{mode}$) differ substantially. In fact, the $T_h$ mode is as poor an estimator of average entrapment conditions as the lowest value in the measured range of $T_h$.

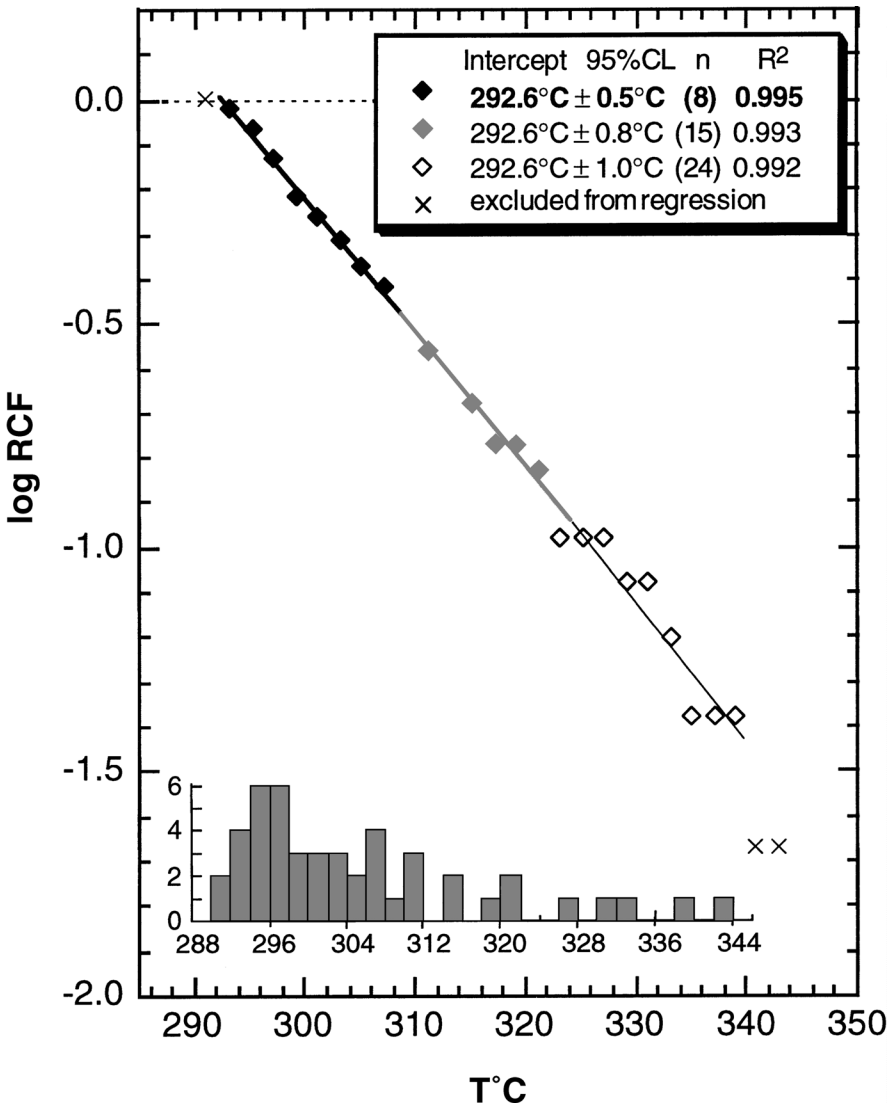


Fig. 14. Illustration of the simple procedure for determining the average entrapment temperature of a population of inclusions that trapped boiling hydrothermal fluids. The data are for secondary fluid inclusions in quartz at 1284 m depth in drill core from an active, and boiling geothermal system supplying electric power in Japan. The raw data as supplied by Sasada, Roedder, and Belkin (1986) are shown as the histogram, binned in 2° intervals. The procedure for data reduction is like that in table 3 and is described in the text. Various continuous subsets of the log RCF vs $T_h$ data array were regressed in successive iterations in order to identify the subset that provides the most robust constraint on the intercept at log RCF = 0 (dashed reference line). That subset of 8 frequency bins (black symbols) gives a coefficient of variation $R^2 = 0.9950$ and a T-axis intercept (= $T_{trap}$) of 292.6° ± 0.5°C at the 95% confidence level (CL), as shown in the inset box. The 292.6° mean $T_{trap}$ differs by ~11 times the standard error from the lowest $T_h$ (290°C) in the measured range, and differs by ~14 times the standard error from the frequency mode of the histogram (296°C), for the reasons illustrated in figure 13. Regression statistics are also shown in the inset box for a "medium" and a "large" subset containing additional points that are shaded grey or blank; the larger subsets include the smaller ones. The reduced $\chi^2 = 1.7$ for the large set (n = 24 frequency bins; all the diamond symbols) indicates that the exponential/logarithmic probability model is an appropriate description of the data.

inclusion attempts to minimize its surface area and energy. Geologic environments in which immiscibility develops are commonly subject to fluctuations of temperature and/or fluid pressure on time scales that are short relative to the duration of crystal growth. A statistically sizable population of fluid inclusions, even along a single growth band of a single crystal, is likely to represent a range of entrapment conditions. Entrapment of mixtures of immiscible fluids within individual inclusions is more prevalent and problematic to accurate geothermometry than has been generally recognized in prior studies. If the analyzed population of primary fluid inclusions was not entrapped precisely synchronously, and if real variations of entrapment temperature–*or some necked inclusions*–are represented in an analyzed population that trapped immiscible fluids, then the procedure of statistical analysis introduced here can discriminate the component of real geologic paleo-temperature variation (and effects of necking) from the variation of homogenization temperature that is due to entrapment of phase mixtures. Necking and real variation of geologic fluid temperature tend to produce a normal-type frequency distribution of $T_h$ and $\rho_B$. Isothermal entrapment of mixtures of immiscible fluids gives rise to *exponential* frequency distributions of $T_h$ and $\rho_B$ in the population of coeval fluid inclusions.

A new data-reduction procedure has been introduced–using the *entire population of measurements*–to identify statistical moments of the exponential distribution by least-squares regression, and extrapolation of the regression trend to its abscissa intercept at RCF = 1.0 to find the limiting value of density or temperature that represents the average entrapment conditions. As demonstrated below, this procedure can improve by at least 10-fold the typical precision of fluid inclusion geothermometry (and hence vapor-pressure paleo-barometry), compared to estimation procedures previously in general use.

## EASY TO USE

In order to provide a reasonably rigorous test of the theoretically postulated exponential distribution, large numbers of inclusions and a statistical analysis of the frequency distribution of fluid-density were used in the illustrative cases with natural fluid inclusions (figure 11). The procedure may have seemed too complicated for "routine use" on the quality of samples usually available. Not so. In this section, I provide a simple demonstration using a smaller dataset produced by other researchers. Datasets as small as 15 penecontemporaneous inclusions are serviceable. Sasada, Roedder, and Belkin (1986) report $T_h$ data for fluid inclusions in quartz from a drill core in an active geothermal system that is producing electric power in Japan. Sasada, Roedder, and Belkin provide persuasive photographic evidence that quartz-hosted fluid inclusions in the upper 1400 m of the core trapped samples of boiling geothermal waters. Their data for a quartz sample at 1284 m depth are shown in histogram form in figure 14. I used that histogram containing 47 $T_h$ values to calculate the fraction of them that fall in each of the 2° bins. The fractional frequency in the highest-temperature bin, 342-344°C is 1/47 = 0.021277, and its logarithm is −1.6721, which is plotted as the lower right endpoint of the array on figure 14. The next interval, 340-342° has a frequency of 0/47, so the *cumulative* frequency in the 340-344° interval is still 1/47, and its log is plotted at T= 341° on figure 14. The interval 338-340° has one inclusion, so the cumulative frequency in the 338-344° interval is 2/47; log (2/47) = −1.3711 is plotted at T=339° on figure 14. And so on down the list. This is easily done in spreadsheet format from a list of $T_h$ values. After generating a plot representing all the histogram bins, a succession of linear regressions of log RCF versus $T_h$ is done for continuous subsets of the data, obtained by iteratively truncating successive points from one or both ends of the $T_h$ range until a subset of the data is identified that gives the most significant (least likely to arise by chance) correlation coefficient, r, and the smallest standard error of the abscissa

intercept. That sample of the dataset is the cleanest representative of the average position and properties of the exponential distribution (compare the shaded squares as a subset of all squares in figure 12). Its regression intercept at log (RCF) = 0.0 on the $T_h$ axis provides the best estimate of the mean $T_{trap}$ of the exponentially distributed fluid inclusion population that trapped immiscible fluids. That value of mean $T_{trap}$ is, of course, also the *mean of the concurrently developed normal distribution* in the analyzed inclusion population (like the midpoint of the data distribution along the horizontal dashed line in figure 12), so the mean $T_{trap}$ and the frequency distribution of $T_h$ values below the mean can be used to quantify the moments of the normal frequency distribution, if it is of interest as an indicator of geologic temperature variation, or whatever meaning the analyst deems appropriate to attach to it.

An additional feature of interest in these data from Sasada, Roedder, and Belkin (1986) is that the fluid inclusions are *secondary* planar swarms. The energetics of vapor nucleation in deep cracks differs in detail from that in shallow, equant pits on the growing crystal surface, so the value of the regression slope cannot be partitioned into energy terms in exactly the same way as in eq (11). (The energetics are also quite different from laboratory synthesis of inclusions in *pre-cracked* quartz.) In the presence of liquid at its boiling temperature, the elastic strain energy released during rupture is available to drive vapor nucleation. In wedge-shaped cracks, the roles of the apical angle $\beta$ and the effective contact angle $\theta'$ are analogous to those illustrated for conical pits in figure 8D, but eq (8) requires modification appropriate to the surface energy of an "infinitely" long two-dimensional liquid-vapor interface having cylindrical rather than spherical curvature.

## POTENTIAL APPLICATIONS OF HIGH-PRECISION GEOTHERMOBAROMETRY

People who use fluid-inclusion thermometry for traditional applications like calculating thermodynamic constraints on compositions of hydrothermal fluids for static descriptions of a particular paragenesis are unlikely to care whether the temperature uncertainty is $\pm 0.5$ or $\pm 5$ to 10°C, because the equilibrium constants for minerals and aqueous complexes and the activity coefficients of solutes in high-salinity fluids often have uncertainties large enough to exceed the influence of a 5 to 10 °C temperature uncertainty.

Of greater interest is that an ability to constrain mineral growth temperatures to $\sim \pm 0.5$°C could permit new applications of fluid-inclusion studies to become routine, such as high-precision vapor-pressure geobarometry for palinspastic reconstructions of structural deformation, by (1) barometric estimation of the vertical component of displacement on faults using samples collected on opposite sides of the displacement surface; or (2) barometric estimation of relative vertical displacements by regional tilting of paleo-isotherms in a region saturated by immiscible fluids. Quadrupole mass-spectrometric analysis of dissolved gases in single inclusions (for example, Graney and Kesler 1995) that trapped only the liquid phase of immiscible hydrothermal fluids has reached a level of analytical precision that can take advantage of a precision of a fraction of a degree in geothermometry in order to achieve geobarometric precision on the order of $\pm 1\%$ of $P_{total}$ or better. Laser-ablation inductively-coupled-plasma mass-spectrometric analysis of dissolved salts in single fluid inclusions (Audétat, Günther, and Heinrich, 1998; Heinrich and others, 1999), for combination with the gas analyses, is an important advance toward recovery of precise paleo-vapor pressures and thermochemical data for minerals. Estimates of fluid composition by micro-thermometry alone are generally far too inaccurate to be useful in exploiting possibilities for reconstructive fluid dynamics and paleo-hydrology of extinct hydrothermal systems through refined characterization of dynamic-fluid-pressure gradients over sampling distances $\leq$100 meters that are often imposed by limitations of accessibility.

With precise compositional analysis, precise geothermometry could improve our understanding of dynamics of hydrothermal systems–for example, by constraining rock permeabilities appropriate for the reconstructed dynamic pressure gradients; for constraining magnitudes and mineralization significance of pressure and temperature transients that accompany seismic faulting; and for characterizing short-term variations as well as secular evolution of the thermal structure of individual hydrothermal systems. Quantification of temperature gradients in the fluid-flow direction is an important missing component of most physico-chemical models of ore-forming processes in particular deposits, with the consequence that cooling is probably undervalued as a genetic process, relative to processes (fluid mixing, gas effervescence, etc.) more readily recognizable by traditional fluid-inclusion petrography and micro-thermometry. Getting precise gradients will generally require correlation of cathodoluminescence or other optical "stratigraphy" of zoned crystals, in combination with high-precision geothermometry.

Much of the available information on stable-isotope fractionation factors among minerals and fluids, and on the molar entropies, enthalpies, and Gibbs energies-of-formation of silicate mineral end-members and their crystalline solutions is based on phase-equilibrium experiments that are restricted to $T \gtrsim 600°C$, because kinetics make equilibration at lower temperatures in the laboratory unfeasible. Chlorites, amphiboles, micas, garnets, pyroxenes, and other minerals of interest in metamorphic and hydrothermal petrology can form under natural conditions ranging down to 300°C or less. A major limitation to using well-equilibrated natural assemblages to extend the calibrations of the thermodynamic properties of minerals to T's below the experimentally tractable range has been uncertainty in the T-P conditions of formation of the natural assemblages. Silicate and oxide mineral assemblages that precipitated from boiling or condensing hydrothermal fluids at shallow depths in porphyry-Cu-Mo-Au, skarn, and epithermal vein deposits tend to cool quickly, quenching-in initial mineral compositions (easily measurable) and preserving in their fluid inclusions a precise record of their T-P-X conditions of formation. The information yield from such assemblages ("natural experiments") could be significantly enhanced by the thermometry techniques introduced here, especially in conjunction with mass-spectrometric analysis of fluid-inclusion compositions.

ACKNOWLEDGMENTS

Andrew Berry, Phil Brown, Larryn Diamond, and Ross Kerr are thanked for comments that improved the clarity of presentation.

REFERENCES

Adamson, A. W., 1990, Physical Chemistry of Surfaces: New York, John Wiley and Sons, Inc., 777 p.

Anderko, A., and Pitzer, K.S. 1993, Equation-of-state representation of phase equilibria and volumetric properties of the system NaCl–$H_2O$ above 573 K: Geochimica et Cosmochimica Acta, v. 57, p. 1657–1680.

Audétat, A., Günther, D., and Heinrich, C. A., 1998, Formation of a magmatic-hydrothermal ore deposit: insights with LA-ICP-MS analysis of fluid inclusions: Science, v. 279, p. 2091–2094.

Benjamin, J. R., and Cornell, C. A., 1970, Probability, Statistics, and Decision for Civil Engineers: New York, McGraw-Hill, 684 p.

Bevington, P. R., 1969, Data Reduction and Error Analysis for the Physical Sciences: New York, McGraw-Hill, 336 p.

Bischoff, J. L., and Pitzer, K. S., 1989, Liquid-vapor relations for the system NaCl-$H_2O$: summary of the P-T-X surface from 300° to 500°C: American Journal of Science, v. 289, p. 217–248.

Bischoff, J. L., and Rosenbauer, R. J., 1985, An empirical equation of state for hydrothermal seawater (3.2 percent NaCl): American Journal of Science, v. 285, p. 725–763.

Blount, C. W., 1977, Barite solubilities and thermodynamic quantities up to 300°C and 1400 bars: American Mineralogist, v. 62, p. 942–957.

Bodnar, R. J., and Bethke, P. M., 1984, Systematics of stretching of fluid inclusions I: Fluorite and sphalerite at 1 atmosphere confining pressure: Economic Geology, v. 79, p. 141–161.

Bodnar, R. J., Burnham, C. W., and Sterner, S. M., 1985, Synthetic fluid inclusions in natural quartz. III. Determination of phase equilibrium properties in the system $H_2O$-NaCl to 1000°C and 1500 bars: Geochimica et Cosmochimica Acta, v. 49, 1861–1873.

Bodnar, R. J., Reynolds, T. J., and Kuehn, C. A., 1985, Fluid-inclusion systematics in epithermal systems, *in* Berger, B.R., and Bethke, P.M. editors, Geology and Geochemistry of Epithermal Systems: Society of Economic Geologists, v. 2, p. 73–97.

Bodnar, R. J., and Sterner, S. M., 1985, Synthetic fluid inclusons in natural quartz. II. Application to PVT studies: Geochimica et Cosmochimica Acta, v. 49, p. 1855–1859.

Chen, C.-T. A., and Marshall, W. L., 1982, Amorphous silica solubilities IV. Behavior in pure water and aqueous sodium chloride, sodium sulfate, magnesium chloride, and magnesium sulfate solutions up to 350°C: Geochimica et Cosmochimica Acta, v. 46, p. 279–287.

Collier, J. G., 1981, Convective Boiling and Condensation: New York, McGraw-Hill, 557 p.

Drummond, S. E., Jr., ms., 1981, Boiling and mixture of hydrothermal fluids: chemical effects on mineral precipitation: Ph.D. Dissertation, Pennsylvania State University, 380 p.

Ellis, A. J., 1963, The solubility of calcite in sodium chloride solutions at high temperatures: American Journal of Science, v. 261, p. 259–267.

Gibbs, J. W., 1906, The Scientific Papers of J. Willard Gibbs, Volume 1, Thermodynamics: London, Longmans Green, 434 p.

Graney, J. R., and Kesler, S. E., 1995, Factors affecting gas analysis of inclusion fluid by quadrupole mass spectrometry: Geochimica et Cosmochimica Acta, v. 59, p. 3977–3986.

Haar, L., Gallagher, J. S., and Kell, G. S., 1984, NBS/NRC Steam Tables: New York, Hemisphere Publishing Corp., 320 p.

Haas, J. L., Jr., 1976, Physical properties of the coexisting phases and thermochemical properties of the $H_2O$ component of boiling NaCl solutions: U.S.Geological Survey Bulletin 1421-A, 73 p.

Heinrich, C. A., Ryan, C. G., Mernagh, T. P., and Eadington, P. J., 1992, Segregation of ore metals between magmatic brine and vapor: a fluid inclusion study using PIXE microanalysis: Economic Geology, v. 87, p. 1566–1583.

Heinrich, C. A., Günther, D., Audétat, A., Ulrich, T., and Frischknecht, R., 1999, Metal fractionation between magmatic brine and vapor, determined by microanalysis of fluid inclusions: Geology, v. 27, p. 755–758.

Helgeson, H.C., 1992, Effects of complex formation in flowing fluids on the hydrothermal solubilities of minerals as a function of fluid pressure and temperature in critical and supercritical regions of the system H2O: Geochimica et Cosmochimica Acta, v. 56, p. 3191–3207.

Helgeson, H. C., Kirkham, D. H., and Flowers, G. C., 1981, Theoretical prediction of the thermodynamic behavior of aqueous electrolytes at high pressures and temperatures: IV. Calculation of activity coefficients, osmotic coefficients, and apparent molal and standard and relative partial molal properties to 600 °C and 5 kb. American Journal of Science, v. 281, p. 1249–1516.

Hendel E. M., and Hollister L. S., (1981) An empirical solvus for $CO_2$-$H_2O$-2.6 wt% salt. Geochimica et Cosmochimica Acta, v.45, p. 225–228.

Johnson, J. S., Oelkers, E. H., and Helgeson, H. C., 1992, SUPCRT92: a software package for calculating the standard molal thermodynamic properties of minerals, gases, aqueous species, and reactions from 1 to 5000 bar and 0° to 1000 °C: Computers and Geosciences, v. 18, p. 899–947.

Kerr, R. C., 1995, Convective crystal dissolution: Contributions to Mineralogy and Petrology, v. 121, p. 237–246.

Lakshtanov, L. Z., Shmonov V. M., Dadze, A., van der Erden, A., and Jansen, B., 1995, Surface free energy in the quartz-water system at high T and P: Geochemistry International, v. 32, p. 51–61.

Lee, V. W., Mackwell, J. S., and Brantley, S. L., 1991, The effect of fluid chemistry on wetting textures in novaculite: Journal of Geophysical Research, v. 96, p. 10023–10037.

Loucks, R. R., Lemish, J., and Damon, P. E., 1988, Polymetallic epithermal fissure vein mineralization, Topia, Durango, Mexico: Part I. District geology, geochronology, hydrothermal alteration, and vein mineralogy: Economic Geology, v. 83, p. 1499–1528.

Oelkers, E. H., and Helgeson, H. C., 1990, Triple-ion anions and polynuclear complexing in supercritical electrolyte solutions: Geochimica et Cosmochimica Acta, v. 54, p. 727–738.

Parks, G. A., 1984, Surface and interfacial free energies of quartz: Journal of Geophysical Research, v. 89, p. 3997–4008.

Pitzer, K. S., and Brewer, L., 1961, Thermodynamics: New York, McGraw-Hill, 694 p.

Pitzer, K. S., Peiper, J. C., and Busey, R. H., 1984, Thermodynamic properties of aqueous sodium chloride solutions: Journal of Physical and Chemical Reference Data, v. 13, p. 1–102.

Pokrovski, G. S., Schott, J., and Sergeyev, A. S., 1995, Experimental determination of the stability constants of $NaSO_4^-$ and $NaB(OH)_4$ in hydrothermal solutions using a new high-temperature sodium-selective glass electrode–implications for boron isotopic fractionation: Chemical Geology, v. 124, p. 253–265.

Potter, R. W. II, Clynne, M. A., and Brown, D. L., 1978 Freezing point depression of aqueous sodium chloride solutions: Economic Geology, v. 73, p. 284–285.

Robert, F., Boullier, A.-M., and Firdaous, K., 1995, Gold-quartz veins in metamorphic terranes and their bearing on the role of fluids in faulting. Journal of Geophysical Research, v. 100, p.12,861–12,879.

Roedder, E., 1967, Fluid inclusions as samples of ore fluids, *in* Barnes, H.L., editor, Geochemistry of Hydrothermal Ore Deposits: New York, Holt, Rinehart, and Winston, p. 515–574.

——— 1972, Composition of fluid inclusions. U.S. Geological Survey Professional Paper 440-JJ, 164 p.

——— 1974, Changes in ore fluid with time, from fluid inclusion studies at Creede, Colorado: Proceedings of the Fourth IAGOD Symposium, Varna, Bulgaria, v. 2, p. 179–185.

——— 1981, Origin of fluid inclusions and changes that occur after trapping, *in* Hollister, L.S., and Crawford, M.L., editors, Short Course in Fluid Inclusions: Applications to Petrology: Mineralogical Association of Canada, p. 101–137.

——— 1984, Fluid Inclusions: Mineralogical Society of America, Reviews in Mineralogy, v. 12, 644 p.

Roedder, E., and Belkin, H. E., 1979, Application of studies of fluid inclusions in Permian Salado salt, New Mexico, to problems of siting the Waste Isolation Pilot Plant, *in* McCarthy, G.J., editor, Scientific Basis for Nuclear Waste Management: New York, Plenum Publishing Corporation , v. 1, p. 313–321.

Sasada, M., Roedder, E., and Belkin, H. E., 1986, Fluid inclusions from drillhole DW-5, Hohi geothermal area, Japan: evidence of boiling and procedure for estimating $CO_2$ content: Journal of Volcanology and Geothermal Research, v. 30, p. 231–251.

Shelton, K. L., and Orville, P. M., 1980, Formation of synthetic fluid inclusions in natural quartz: American Mineralogist, v.65, p. 1233–1236.

Sourirajan, S., and Kennedy, G. C., 1962, The system $H_2O$–NaCl at elevated temperatures and pressures: American Journal of Science, v. 260, p. 115–141.

Sverjensky, D. A., Shock, E. L., and Helgeson, H. C., 1997, Prediction of the thermodynamic properties of aqueous metal complexes to 1000°C and 5 kb: Geochimica et Cosmochimica Acta, v. 61, p. 1359–1412.

Vikre, P. G., 1985, Precious metal vein systems in the National district, Humbolt County, Nevada: Economic Geology, v. 80, p. 360–393.

Volmer, M., 1929, Uber Keimbildung und Keimwirkung als Spezialfälle der heterogenen Katalyse: Zeitschrift für Elektrochemie, v. 35, p. 555–561.

Werre, R. W., Jr., Bodnar, R. J., Bethke, P.M., and Barton, P. B., Jr., 1979, A novel gas-flow fluid inclusion heating/freezing stage [abstract]: Geological Society of America Abstracts with Program, v. 11, p. 539.

Yardley, B. W. D., and Bottrell, S. H., 1988, Immiscible fluids in metamorphism: implications of two-phase flow for reaction history: Geology, v. 16, p. 199–202.

Zhang, Y., 1998, Mechanical and phase equilibria in inclusion-host systems: Earth and Planetary Science Letters, v. 157, p. 209–222.